iScience

CellPress

Article

Electrically Sorted Single-Walled Carbon Nanotubes-Based Electron Transporting Layers for Perovskite Solar Cells

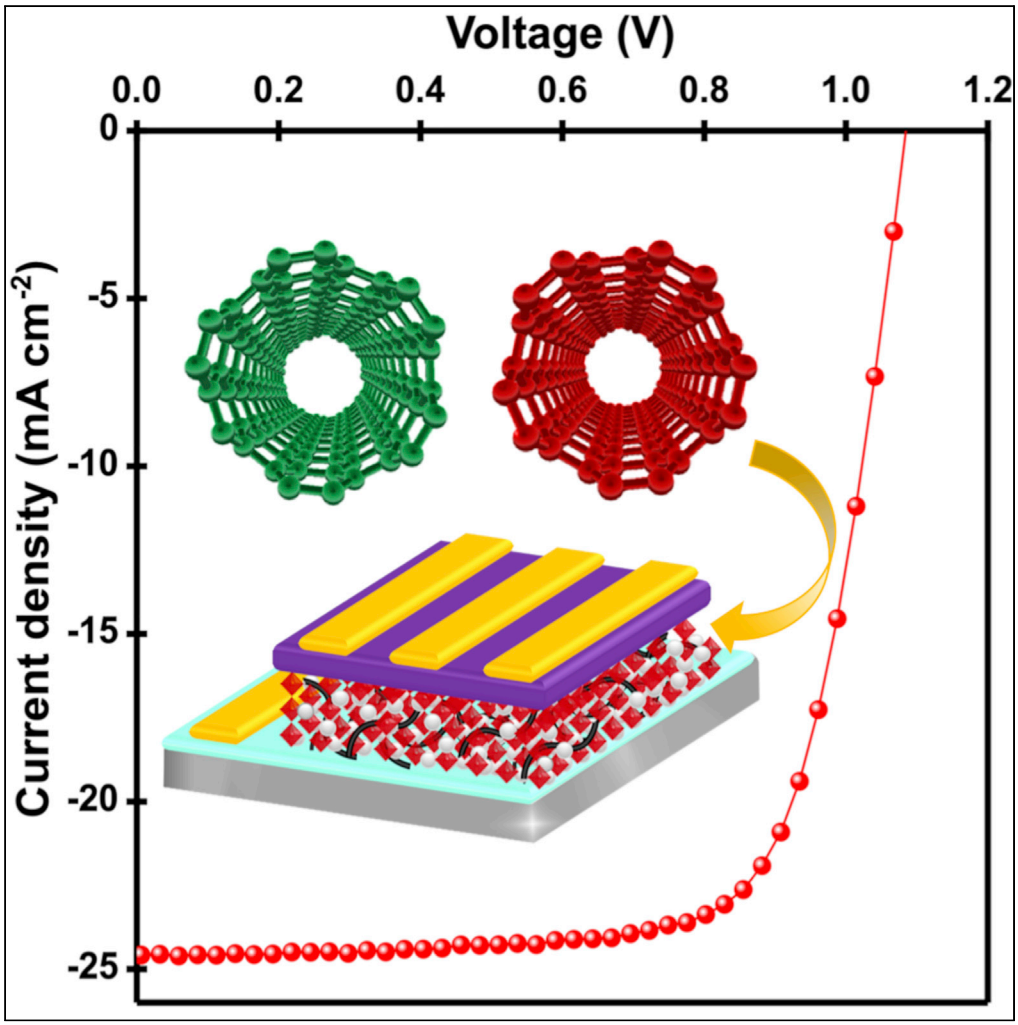

Abdulaziz S.R. Bati, LePing Yu, Sherif Abdulkader Tawfik, Michelle J.S. Spencer, Paul E. Shaw, Munkhbayar Batmunkh, Joseph G. Shapter

j.shapter@uq.edu.au

HIGHLIGHTS

PSCs based on ETLs containing separated families of SWCNTs are fabricated

Nanotube compositions are precisely tuned to enable the highest PCE

By optimizing the nanotube ratio, an efficiency of 19.35% is obtained

Elucidation of the optimal ratio of s-SWCNTs vs. m-SWCNTs for charge transport electrodes

Bati et al., iScience *14*, 100–112
April 26, 2019
https://doi.org/10.1016/j.isci.2019.03.015

iScience

CellPress

Article

Electrically Sorted Single-Walled Carbon Nanotubes-Based Electron Transporting Layers for Perovskite Solar Cells

Abdulaziz S.R. Bati,[1] LePing Yu,[2] Sherif Abdulkader Tawfik,[3] Michelle J.S. Spencer,[3] Paul E. Shaw,[4] Munkhbayar Batmunkh,[1,2] and Joseph G. Shapter[1,2,5,*]

SUMMARY

Incorporation of as prepared single-walled carbon nanotubes (SWCNTs) into the electron transporting layer (ETL) is an effective strategy to enhance the photovoltaic performance of perovskite solar cells (PSCs). However, the fundamental role of the SWCNT electrical types in the PSCs is not well understood. Herein, we prepared semiconducting (s-) and metallic (m-) SWCNT families and integrated them into TiO_2 photoelectrodes of the PSCs. Based on experimental and theoretical studies, we found that the electrical type of the nanotubes plays an important role in the devices. In particular, the mixture of s-SWCNTs and m-SWCNTs (2:1 w/w)-based PSCs exhibited a remarkable efficiency of up to 19.35%, which was significantly higher than that of the best control cell (17.04%). In this class of PSCs, semiconducting properties of s-SWCNTs play a critical role in extracting and transporting electrons, whereas m-SWCNTs provide high conductance throughout the electrode.

INTRODUCTION

Organic–inorganic halide perovskite solar cells (PSCs) have received a great deal of attention from the photovoltaic (PV) community owing to the remarkable progress in the performance, which has recently exceeded 23% (National Renewable Energy Laboratory, 2019). Hybrid perovskite-based light absorbers exhibit an outstanding combination of desirable properties, including high absorption coefficients, high ambipolar carrier transport, and long charge-diffusion lengths, in addition to their attractive features such as ease of fabrication, low cost, and rigid/flexible substrate compatibility (Park, 2013; Ball et al., 2013; Green et al., 2014; Cai et al., 2017; Petrus et al., 2017). A typical state-of-the-art PSC that exhibits high device efficiency consists of a transparent conducting oxide substrate, compact layer, semiconducting metal oxide scaffold layer, perovskite light absorber, hole transporting layer (HTL), and metal electrode. In such a device architecture, the semiconducting metal oxide nanoparticles (NPs) play an important role in extracting and transporting electrons from the perovskite to the conductive electrode (Kim et al., 2014; Edri et al., 2014). The most commonly used electron transporting material (ETM) is the semiconducting metal oxide TiO_2. TiO_2 nanostructure materials have been intensively used in various applications such as photovoltaics (Bai et al., 2014) and photocatalysis (Nakata and Fujishima, 2012; Woan et al., 2009) because of their good chemical stability, wide band gap, lack of toxicity, and high transparency (He et al., 2014). However, the TiO_2-based ETM suffers from intrinsic drawbacks including low electron mobility, numerous grain boundaries, and heterogeneous spreading of TiO_2 nanocrystallite network, which introduces a random transit path for the electrons, leading to rapid charge recombination and thus a deterioration of device performance (Kim et al., 2009). Therefore, there is a real necessity to discover and investigate alternative materials to replace or improve the properties of TiO_2-based ETM for further enhancement in the PCE of the PSCs. In this context, various highly conducting carbon-based nanomaterials such as graphene and its derivatives (Han et al., 2015; Agresti et al., 2016; Wang et al., 2013), fullerenes (Wojciechowski et al., 2014; Hou et al., 2018; Yoon et al., 2016), and carbon nanotubes (Habisreutinger et al., 2014b, 2017; Li et al., 2014; Luo et al., 2017b, 2018) have been widely used in PSCs and are recognized as promising candidates to facilitate charge extraction/transportation and extend electron lifetime. Among these nanomaterials, SWCNTs have shown remarkable properties, such as high aspect ratio, excellent electron mobility, high chemical stability, outstanding mechanical and thermal properties, high transparency, and suitable electronic structure (Zhou et al., 2009), making them ideal for improving the performance of PSCs (Aitola et al., 2016; Jeon et al., 2015; Li et al., 2016). Recently, our group reported for the first time the successful fabrication of efficient PSCs by incorporating SWCNTs into the TiO_2 photoelectrodes (Batmunkh et al.,

[1]Australian Institute for Bioengineering and Nanotechnology, The University of Queensland, Brisbane, QLD 4072, Australia

[2]College of Science and Engineering, Flinders University, Adelaide, SA 5042, Australia

[3]School of Science, RMIT University, GPO Box 2476, Melbourne, VIC 3001, Australia

[4]School of Chemistry and Molecular Biosciences, The University of Queensland, Brisbane, QLD 4072, Australia

[5]Lead Contact

*Correspondence: j.shapter@uq.edu.au

https://doi.org/10.1016/j.isci.2019.03.015

2017b). This work highlights the potential of SWCNTs to enhance the properties of the electron transporting layer (ETL) in PSCs. It is worth noting that pristine SWCNTs (p-SWCNTs) (before separation) are commercially available as a mixture of two-thirds semiconducting (s-SWCNTs) and one-third metallic (m-SWCNTs) nanotubes. Such a variation in the nanotube properties is detrimental to device performance and reproducibility. Driven by the recent advances made in the separation and controlled growth methods of SWCNTs, it is now viable to tailor the optoelectronic properties of this fascinating material to maximize the charge extraction and transport in PSCs (Bati et al., 2018). For example, Snaith's group employed a double HTL composed of P3HT-SWCNTs network and poly(methyl methacrylate) (PMMA) matrix (Habisreutinger et al., 2014a). Comparing the performance of the devices when the as-produced SWCNTs (2:1 s-:m-SWCNTs) were replaced with highly enriched m-SWNTs, an improvement was evident boosting the PCE from a maximum of 14.2% to 15.3%. This efficiency improvement is attributed to the conductivity enhancement resulting from the incorporation of m-SWCNTs with their high conductivity as compared with their s-SWCNTs counterparts. Blackburn and co-workers reported the improved efficiency, stability, and reduced hysteresis when a pure s-SWCNTs layer highly enriched with (6,5) nanotubes was inserted as an interfacial layer between the perovskite layer and Spiro-OMeTAD (Ihly et al., 2016). The PCE of such a device configuration exhibited a dramatic improvement from 14.7% to 16.5%.

Although PSCs based on TiO_2 with pristine SWCNTs incorporated have shown improved performance and stability, a crucial fundamental question regarding whether integrating a pure single electronic-type SWCNT into the TiO_2 photoelectrodes would provide better charge transfer still remains. Moreover, further insight into the effect of the distribution of carbon nanotube (CNT) electronic types would be very valuable.

Herein, we report the implementation of SWCNTs separated by electrical type (i.e., semiconducting and metallic) into TiO_2 at precisely tuned ratios as an efficient ETL for PSCs. At the optimum SWCNT loadings, notable enhancement in the PV efficiency was achieved regardless of the nanotube types incorporated. Interestingly, (2:1 w/w) s-:m-SWCNTs showed a remarkable PCE of 19.35%, whereas the best performing TiO_2-only reference device exhibited an efficiency of 17.04%. This significant efficiency enhancement is attributed to the reduced charge transfer resistance (R_{ct}) resulting from the favorable energy level alignment at the perovskite/ETL interface. In addition, our devices with nanotubes showed improved stabilities under continuous light illumination in ambient environment and exhibited less hysteresis behavior.

RESULTS AND DISCUSSION

Owing to its simplicity, short preparation time requirements, cost-efficiency, scalability, and the high purity of the separated samples, a column gel chromatographic method was used to prepare SWCNT suspensions enriched in either m- or s-SWNTs (Tanaka et al., 2009). A schematic diagram of the separation process is shown in Figure S1.

The obtained SWCNT solutions exhibited two distinct colors, indicating successful enrichment of s- and m-SWCNTs fractions. The proportions of s- and m-SWCNTs in the samples were estimated as described by Ao et al. (2014). The integrated areas of the first transition of s-SWCNTs ($S_{11,}$ ~950–1,350 nm) and m-SWCNTs (M_{11}, ~450–650 nm) (Tanaka et al., 2009) between van Hove singularities (vHs) in the density of states (DOS) were used as a guide for the concentration estimation. We assume that 1 absorption unit (with 1 cm optical path length) at S_{11} corresponds to 5 μg mL^{-1} for s-SWCNTs, whereas 1 absorption unit at M_{11} corresponds to 15 μg mL^{-1} for m-SWCNTs. A wide range of s-: m-SWCNTs ratios were combined in an appropriate volume.

Figure 1A shows the optical absorption spectra of pristine SWCNTs (p-SWCNTs) and separated SWCNTs at different s- and m-SWCNTs ratios of 1:0, 0:1, 2:1, 1:2, and 1:1 (w/w). The typical s-SWCNTs peaks (S_{11}, S_{22}, S_{33}) and m-SWCNTs (M_{11}) can be clearly observed from the spectra depicted in Figure 1A. By varying s- and m-SWCNT content, the increment and decrement in their related peaks with respect to the p-SWCNTs can be clearly seen, indicating effective control over their ratios. Resonance Raman spectroscopy was used to evaluate s- and m-SWCNTs separation and to investigate the variation of their signals that contain both fractions as illustrated in Figures 1B and 1C. The three Raman peaks centered at ~1,590, ~1,560 and ~200 cm^{-1} are typical peaks for SWCNTs assigned to the G^+, G^- modes and radial breathing mode (RBM), respectively. These distinct features can be used to determine the enrichment levels of metallic and semiconducting nanotubes and track any changes in their ratios (Jorio et al., 2003). As compared

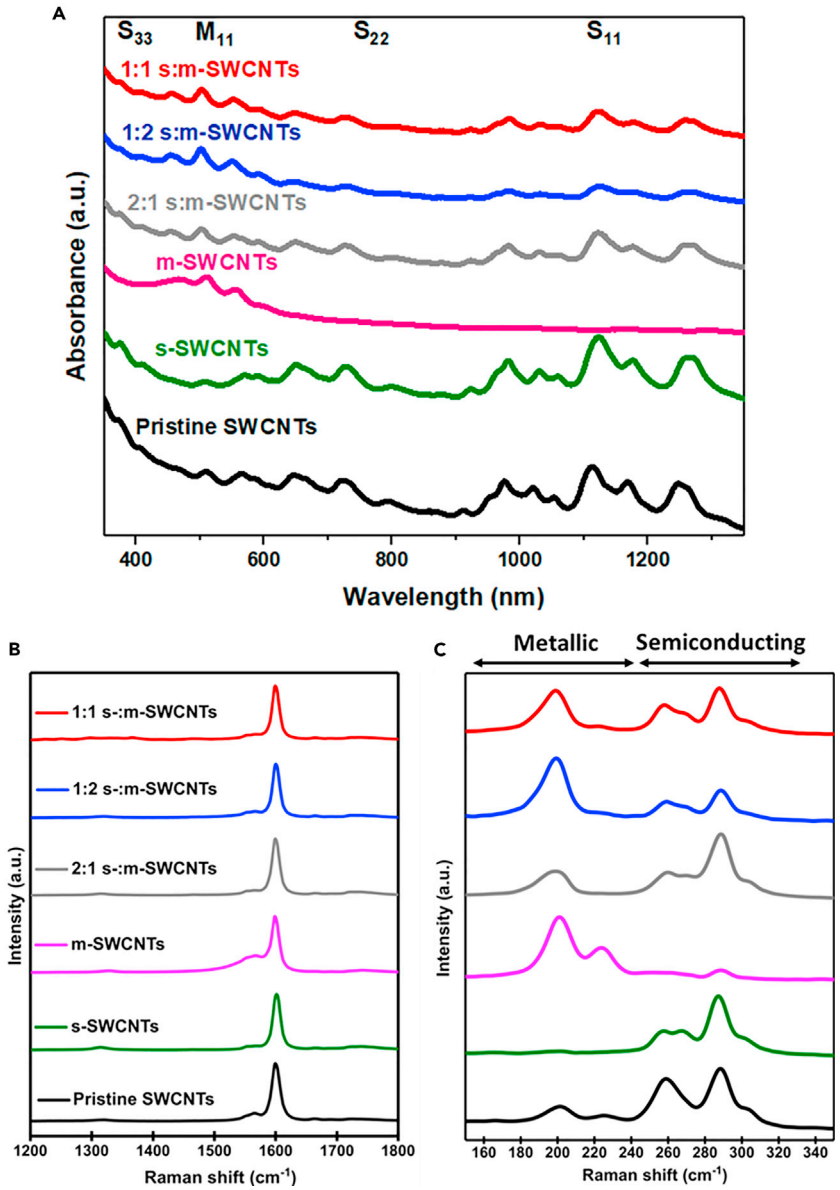

Figure 1. Optical Characterization of the Prepared SWCNTs Solutions

(A) Optical absorbance spectra, (B) resonance Raman spectra, and (C) RBM from Raman spectra of pristine, s-SWCNTs, m-SWCNTs, and a mixture of s-SWCNTs and m-SWCNTs species with different weight ratios of 2:1, 1:2, and 1:1.

with the Lorentzian-like line shape of s-SWCNTs, the G^- band shape of m-SWCNTs is broadened (Breit-Wigner-Fano line shape) owing to the presence of high fractions of metallic nanotubes with a high number of free electrons (Singh et al., 2009). In addition, the RBM peaks, shown in Figure 1C, demonstrate the high purity of the separated s- and m-SWCNTs fractions. Figure 1C also indicates the successful tuning of both m- and s-SWCNT ratios with the changes in the band intensities. The surface morphology of p-, s-, and m-SWCNTs was investigated using a scanning electron microscopy (SEM) (Figure S2). Since the separation procedure was carried out based on the electronic characteristic difference between s- and m-SWCNTs, no significant difference in the surface morphological features were observed.

Various SWCNTs/TiO_2 NPs composites were prepared by adding different SWCNT loadings with controlled ratios of nanotube types. The loading of SWCNTs in the composite was varied from 0.05 to 0.50 wt%. The morphology of the TiO_2/SWCNTs composite was characterized using SEM and transmission

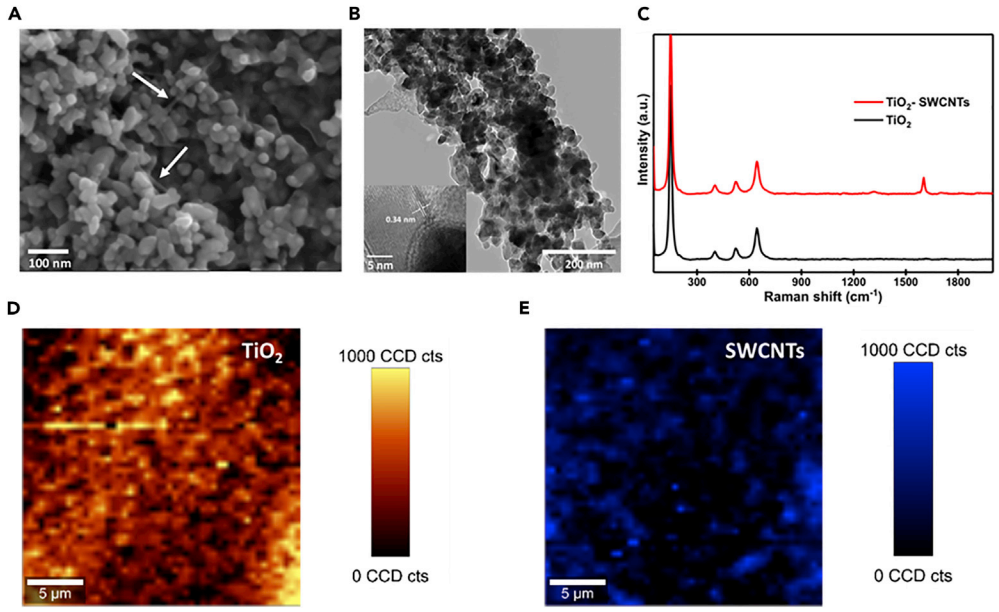

Figure 2. Surface Characteristics of the TiO_2/Nanotubes Composite

(A) Top-view SEM image and (B) TEM image of the TiO_2/nanotubes composite. Inset shows the lattice fringes of the SWCNTs.

(C–E) (C) Raman spectra of the bare TiO_2 and TiO_2/SWCNTs composite. Raman spectra mapping showing the distribution of (D) TiO_2 NPs (orange) and (E) SWCNTs in the composite (blue). The color scale bar at the right side of each image represents the signal intensity of the TiO_2 NPs and SWCNTs.

electron microscopy (TEM), where the well-embedded CNTs within the TiO_2 matrix can be clearly seen (Figures 2A and 2B). The spacing between the lattice fringes was measured to be 0.34 nm, which is consistent with the reported value for SWCNTs (Qian et al., 2002). The existence of the nanotubes was further supported by the Raman spectra as shown in Figure 2C. The four peaks appearing at ~ 150, 398, 518, and 641 cm^{-1} can be assigned to the characteristic peaks for the anatase phase of TiO_2 (Ohsaka et al., 1978). The observed SWCNT peak at 1,600 cm^{-1} in the Raman spectra alongside the TiO_2 peaks confirms the presence of the nanotubes in the TiO_2 matrix. In addition, the distribution of the SWCNTs throughout the TiO_2 matrix was further investigated. Figures 2D and 2E show confocal Raman mapping, which reveals the uniformly dispersed SWCNTs in the TiO_2 matrices.

To evaluate the effect of different types of electrically sorted SWCNTs on the performance of the mesoscopic PSCs, devices with the structure illustrated in Figure 3A were fabricated. A cross-sectional SEM image of the fabricated PSCs is presented in Figure 3B.

To optimize the device performance, SWCNT loadings in the mesoporous TiO_2 were varied from 0 to 0.50 wt%. The corresponding PV parameters, including the short-circuit current (J_{sc}), open-circuit voltage (V_{oc}), fill factor (FF), and PCE as a function of different SWCNT content, are illustrated in Figures S3–S7. As can be seen in Figures S3–S7, regardless of the nanotube type/composition, there is a clear trend between the SWCNT loadings and efficiency enhancement for all TiO_2/SWCNTs-based PSCs. The best control device with no SWCNTs delivered a PCE of 17.04% with J_{sc} of 22.50 mA cm^{-2}, V_{oc} of 1.046 V, and FF of 0.72. Upon increasing the SWCNT concentration, remarkable improvements in the PCEs were observed. In particular, the 2:1 s-:m-SWCNTs at the loading of 0.40 wt% showed the highest PCE of 19.35% with J_{sc} of 24.59 mA cm^{-2}, V_{oc} of 1.085 V, and FF of 0.73. After further increasing the SWCNT loading to 0.50 wt%, the PCEs started to decrease to a maximum PCE of 16.39%. For PSCs with only s-SWCNTs, only m-SWCNTs, 1:2 and 1:1 (s-:m-SWCNTs), similar trends were observed; maximum PCE values of 18.10%, 17.77%, 17.21%, and 18.09%, respectively, were observed.

Although all PV parameters improved to varying degrees with the addition of SWCNTs, the major PV parameters leading to improved efficiencies were J_{sc} and FF. This can be ascribed to the enhanced electron

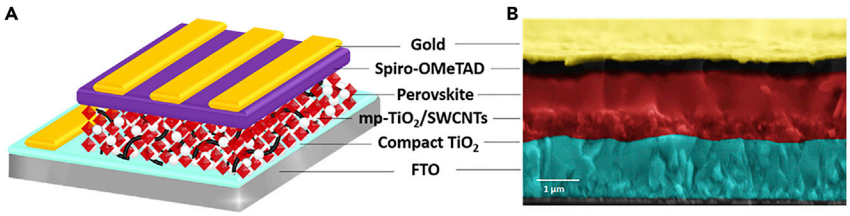

Figure 3. Architecture of the Fabricated Devices

(A) Schematic diagram of the structure of PSCs, where CNTs (black lines) were incorporated into the TiO_2 mesoporous scaffold layer.

(B) Cross-sectional SEM image of the complete device.

extraction and reduced charge recombination rates (Agresti et al., 2016; Kim et al., 2016; Wang et al., 2015). Clearly the SWCNTs have a significant role in collecting and transporting the photogenerated electrons from the perovskite to the conductive electrodes. However, when the optimum concentration of SWCNTs in the composite is exceeded, the device performances started to decrease. Given the ability of SWCNTs to conduct both electrons and holes, obtaining an optimal concentration is of great importance (Batmunkh et al., 2017a). When the concentration of the SWCNTs in the composite is too high, significant charge recombination between the SWCNTs and perovskite is likely to occur because of the direct contact between them (Wang et al., 2013). On the other hand, when the SWCNT loading is small and/or optimal, the nanotubes in the composite are fully covered by the TiO_2 NPs, which will prevent the direct contact between the SWCNTs and perovskite, minimizing the charge carrier losses (Batmunkh et al., 2015). The current density – voltage (J–V) curves of the champion PSCs measured under 100 mW cm^{-2} air mass 1.5 global (AM 1.5G) are displayed in Figure 4, and their corresponding parameters have been summarized in Table 1. As can be seen in Table 1, TiO_2/m-SWCNTs-based devices showed decreased J_{sc} as compared with other devices, which could be ascribed to two factors: (1) m-SWCNTs/TiO_2 junctions exhibit insufficient built-in potential that was theoretically estimated to be 0.09 eV resulting in lower driving force for charge separation. This value is much lower than that of s-SWCNTs/TiO_2 junctions found to be 0.65 eV (Long, 2013). (2) The high rate of back electron transfer originated from the continuous energy levels near the Fermi level of m-SWCNTs can accelerate the charge recombination process, which agrees well with other studies (Dang et al., 2011).

It is noteworthy that the devices containing nanotubes exhibit higher V_{oc} than those based on TiO_2 only ETLs. The changes in V_{oc} have been observed previously with the addition of nanotubes and can be traced to slight shifts in the TiO_2 conduction band levels (Batmunkh et al., 2017a; Macdonald et al., 2015). Since the V_{oc} in PSCs is defined as the energy difference between the conduction band minimum (CBM) of the ETL and the valance band maximum of the perovskite (Ke et al., 2016), and considering the fact that only the ETLs were modified, we can safely conclude that the integration of SWCNTs into the TiO_2 photoelectrodes leads to a better interfacial band alignment between the ETL and the perovskite layer.

To study the J_{sc} changes after integrating different types of SWCNTs, the external quantum efficiency (EQE) spectra of the devices were collected and plotted (Figure 5A). The integrated photocurrent densities from EQE measurements were 20.43, 20.84, 20.47, 21.72, 20.06, and 21.12 mA cm^{-2} for the devices based on TiO_2 NPs-only, s-SWCNTs, m-SWCNTs, 2:1, 1:2 and 1:1 s-:m-SWCNTs, respectively, which are in good agreement (within $\pm$10% error) with the average corresponding J_{sc} values obtained from the J-V measurements. Enhancements in the EQE spectra as compared with the control device over the entire wavelength region for PSCs based on 2:1 and 1:1 (s-: m-SWCNTs) were observed. In particular, the markedly improved EQE of the 2:1 s-:m-SWCNTs-based device in the long wavelength region (480 and 750 nm) is noteworthy. We attribute this to the superior charge injection/collection properties in the presence of 2:1 s-:m-SWCNTs. In principle, longer wavelength corresponds to the lower energy photogenerated electrons. As such, the probability of these electrons being trapped before being injected into the ETL is high (Agresti et al., 2016). However, when SWCNTs are incorporated into the TiO_2 in a proper ratio and optimum concentration, their smaller band gap relative to the TiO_2, favorable energetic alignment, and their high conductivity can effectively extract and collect the photoinduced electrons. On the other hand, other devices such as only s-SWCNTs and m-SWCNTs showed some improvements in the EQE spectra only in the short wavelength region (~350–550 nm). In general, the introduction of CNTs into the TiO_2 is expected to improve

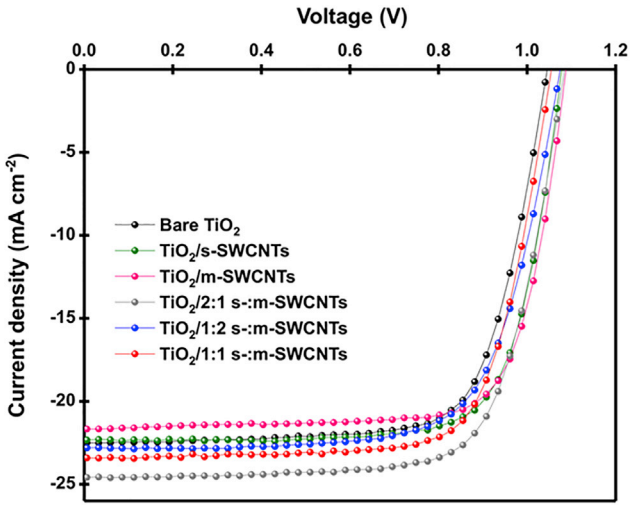

Figure 4. *J-V* Curves of the Best Performing Devices Fabricated Based on Various TiO_2/SWCNTs Composite Photoelectrodes Measured under 1 Sun Illumination Condition (AM 1.5 G)

the interconnection of the TiO_2 grains. Such an effective approach can result in a larger interfacial area between the TiO_2 NPs leading to a reduced number of grain boundaries and charge recombination, hence improving charge collection.

To gain further insights into the influence of different SWCNT types in the fabricated devices, electrochemical impedance spectroscopy (EIS) was carried out. Figure 5B shows the Nyquist plots of bare TiO_2 NPs and various TiO_2 NPs-SWCNTs photoelectrode-based PSC devices alongside the equivalent circuit used to fit the spectra. The measurements were carried out at room temperature at 0.8 V bias voltage under light conditions. In a typical Nyquist plot, two circular arc features are observed. It is well known that the first semicircle at the higher frequency is related to the charge transfer resistance (R_{ct}), whereas the second semicircle at the lower frequency can be associated with the charge recombination resistances (R_{rec}) at the ETL/perovskite interface (Zhu et al., 2018). The R_{rec} is inversely proportional to the recombination rate of the charge carriers (Zhu et al., 2018). In this study, we focused on evaluating the R_{ct} of the devices. The measured R_{ct} values of the PSCs with bare TiO_2, s-,m-, 2:1 s-:m-, 1:2 s-:m-, and 1:1 s-:m-SWCNTs were 513, 130, 160, 90.5, 260, and 169 Ω, respectively. This reveals that the type of SWCNTs incorporated into the TiO_2 has a direct and indeed considerable influence on the R_{ct} of the PSCs. We attribute the extremely low R_{ct} value for the TiO_2/2:1 s-:m-SWCNTs-based PSCs to the enhanced electron transport caused by the unique combinations of both types of SWCNTs. It has been previously demonstrated that increasing the content of m-SWCNTs to a certain level (~30%) reduces the film resistivity (Blackburn et al., 2008). However, the resistivity showed a dramatic increase when the content of m-SWCNTs is further increased, which demonstrates the important roles played by both electronic types in the charge transport process. Briefly, although the s-SWCNTs with certain energy band gaps are critical in suppressing the device charge recombination by inhibiting the back electron transfer, the high electron conductivity of the m-SWCNTs significantly increases the charge transfer properties of the devices (McEuen and Park, 2004). However, when the content of m-SWCNTs is too high, the back electron transfer rate is increased, leading to high recombination and thus resulting in poor performance. It is worth noting that the reduced R_{ct} for all the devices with SWCNTs incorporated (regardless of their ratios) can be partially ascribed to the improved band alignment of the ELT/perovskite interface. This is in excellent agreement with our previous investigation where the CBM of the TiO_2 was found to be upshifted when SWCNTs are introduced leading to more suitable band alignment with the perovskite, which in turn can facilitate charge injection and transport (Batmunkh et al., 2017a).

The J-V characteristics under dark conditions provide useful information about the charge recombination loss and the leakage current in the devices (Wetzelaer et al., 2015; Yu et al., 2018). As can be clearly seen from the dark J-V curves shown in Figure S8A, all nanotubes-based devices show relatively low leakage current at the reverse bias region ($V < 0$). Notably, the devices fabricated based on solely s-SWCNTs exhibit

Type	J_{sc} [mA cm^{-2}]	V_{oc} [V]	FF	PCE [%]
Bare TiO_2	**22.509** 21.90 ± 0.83	**1.046** 1.053 ± 0.007	**0.72** 0.72 ± 0.01	**17.04** 16.64 ± 0.60
TiO_2/s-SWCNTs	**22.33** 21.99 ± 0.29	**1.080** 1.075 ± 0.005	**0.75** 0.74 ± 0.01	**18.10** 17.60 ± 0.43
TiO_2/m-SWCNTs	**21.677** 21.445 ± 0.37	**1.088** 1.066 ± 0.019	**0.75** 0.74 ± 0.01	**17.77** 17.09 ± 0.70
TiO_2/2:1 s:m-SWCNTs	**24.592** 24.185 ± 0.41	**1.085** 1.074 ± 0.015	**0.73** 0.71 ± 0.02	**19.35** 18.44 ± 0.89
TiO_2/1:2 s:m-SWCNTs	**22.803** 22.52 ± 0.25	**1.075** 1.07 ± 0.004	**0.70** 0.70 ± 0.01	**17.21** 16.86 ± 0.48
TiO_2/1:1 s:m-SWCNTs	**23.411** 22.80 ± 0.56	**1.055** 1.072 ± 0.017	**0.73** 0.73 ± 0.01	**18.09** 17.93 ± 0.14

Table 1. Detailed Average PV Parameters Based on Various TiO_2/SWCNTs Composite Photoelectrodes (Based on at Least 3 Devices) and PV Parameters of the Best Performing Devices (in Bold)

the lowest leakage current followed by the other nanotubes containing devices with less pronounced differences. These results suggest that the leakage current paths can be largely suppressed by the improved charge transport efficiency at the ETL/perovskite interface when s-SWCNTs are integrated into the TiO_2 photoelectrodes, as expected. Similarly, s-SWCNTs-based devices showed an improvement in the current injection under the forward bias indicating reduced charge recombination loss, which is in agreement with our electrochemical impedance spectroscopy analysis. In contrast, a considerable decrease in the current injection of m-SWCNTs-based devices is apparently reflecting serious back recombination between the photogenerated charge carriers at the interface. It is worth mentioning that the absence of a minimum current density at 0 V may be attributed to the fast scan measurements (200 mV s^{-1} in our work) and/or arise from the *J–V* hysteresis. (Hendriks et al., 2017; Sadollahkhani et al., 2017; Peng et al., 2017). To gain further insight into the recombination dynamics of the devices, the ideality factor and saturation current (J_{sat}) are extracted and have been plotted in Figures S8B and S8C. As expected, the ideality factor of the s-SWCNTs was significantly lower than that of the m-SWCNTs with an average of 1.34, whereas increasing the m-SWCNTs content in the photoelectrodes leads to a dramatic increase in the ideality factor reaching an average value of up to 1.72. Such an increase in the ideality factor is a clear indication of increasing the charge recombination rate in the devices confirming the detrimental role of m-SWCNTs when introduced to the TiO_2 photoelectrodes at high concentrations (a value of 1 indicates the full absence of charge carrier recombination in the diode, whereas the recombination process becomes dominant with an ideality factor of 2). Similarly, the J_{sat} values of the PSCs fabricated with s-SWCNTs in the photoelectrodes are low, whereas the devices with increased m-SWCNTs contents show much higher J_{sat}. The reduced ideality factor and J_{sat} of the dominating s-SWCNTs-based devices confirm the importance of the intrinsic band gaps in s-SWCNTs to effectively block the charge back transfer, which can largely reduce the recombination process, thus improving the performances of the devices.

To further investigate the effect of the types of SWCNTs on charge-transfer kinetics and interfacial charge extraction process, time-resolved photoluminescence (TRPL) measurements were carried out. Figure S8D shows the TRPL decays of the perovskite deposited on various substrates, including glass, glass/TiO_2, and glass/TiO_2 with different types of SWCNTs. Briefly, the TiO_2/(2:1) s-:m-SWCNTs-based film exhibited the shortest decay time, which implies more efficient extraction of electrons from the perovskite into the ETL as compared with other films. We attribute this enhancement to the improved electron extraction of the electrode in the presence of both semiconducting and metallic nanotubes. The reduction in non-radiative recombination in the perovskite film due to the suppression of back electron transfer by the semiconducting nanotubes plays an important role while metallic nanotubes provide high electrical conductance.

To understand the effect of the interaction between the CNTs and the anatase surface on their electronic structure, we performed density functional theory (DFT) calculations. We constructed two computational supercells: the (6,5) semiconducting CNT and the (6,3) semi-metallic CNT, each layered on the TiO_2(101)

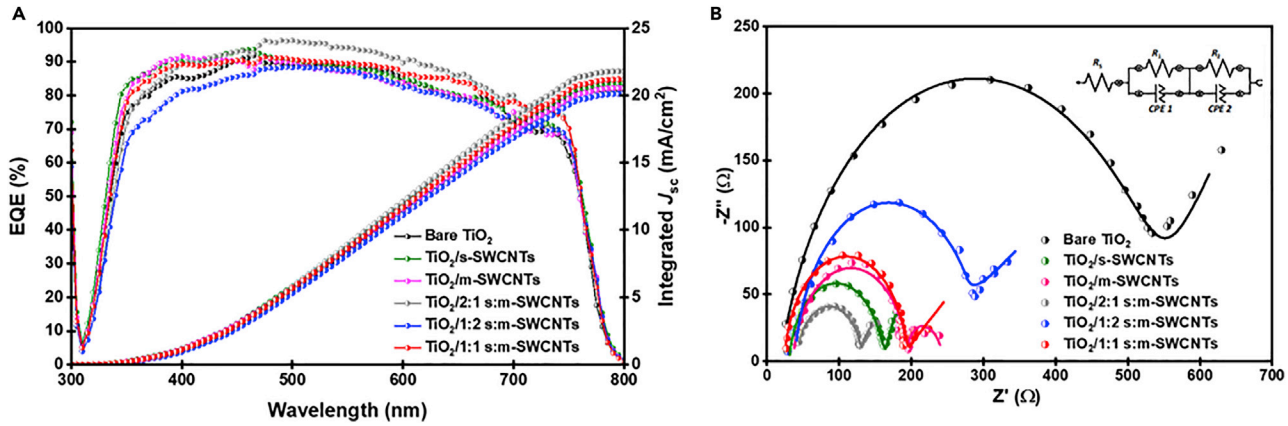

Figure 5. Evaluation of Charge Collection Efficiency and Transportation

(A) EQE spectra and (B) EIS plots for the PSCs based on various photoelectrodes with and without SWCNTs.

anatase surface, as shown in Figure 6. The details of the calculations are described in the Supplemental Information. The band gap obtained for the isolated (6,5) SWCNT is 1.07 eV, whereas that of the TiO_2(101) surface is 2.31 eV, both of which are lower than the experimental values, owing to the tendency of DFT to underestimate the band gap.

For the (6,5) CNT-TiO_2(101) interface, the PV efficiency can be understood in the light of the analysis of the partial density of states (PDOS), as displayed in Figure 7A. In this figure, the density of states of each subsystem is plotted separately. Given that the interaction between the two systems is weak, the electronic density of each subsystem is not affected by the interaction. However, the interaction gives rise to a band alignment, in which the CBM of the (6,5) CNT is higher than that of the TiO_2(101) surface. This implies that an excited electron in (6,5) CNT can experience a transition to the TiO_2(101) surface.

For the (6,3) semi-metallic CNT-TiO_2 (101), we can observe from Figure 7B that the PDOS of the TiO_2 is slightly distorted (compared with that shown in Figure 7A). This distortion indicates the presence of charge transfer across the vacuum gap in the interface. By calculating the charge transfer by using the Voronoi deformation density method (details in the Supplemental Information), we find that a charge of 0.15 |e| is transferred from the CNT to the anatase surface, per computational supercell (that is, 0.002 |e|/carbon atom). This calculated charge transfer explains the impact of using (semi)metallic CNTs as an additive to the TiO_2 on the total performance of the devices: the (semi)metallic CNTs accelerate the injection of electrons into the anatase surface.

The results of these calculations suggest that the conduction band of s- and m-SWCNTs occupy energetically favored sites near the conduction band of the perovskite providing ideal pathways to facilitate electron transportation toward the FTO electrode, where nanotubes can act as a bridge between the perovskite and TiO_2 (Figures 7C and 7D).

The issues associated with the hysteresis behavior and lifetime of PSCs are the major challenges that must be addressed before this cutting-edge technology can be commercialized. The variation in the *J-V* characteristics measurements between the reverse scan direction (V_{oc} to J_{sc}) and forward scan direction (J_{sc} to V_{oc}) can lead to inaccurate evaluation of the device performance (Chen et al., 2016). Although the origin of the hysteresis is not fully understood, early studies suggested that the hysteresis effect of solar cells is attributed to the imperfect contact and charge/ion accumulation at the ETL/perovskite interface (Jeon et al., 2014; Ke et al., 2015). Indeed, the replacement/incorporation of various materials as an efficient ETL has greatly minimized the hysteresis of PSCs, which can support this hypothesis (Ke et al., 2015; Hu et al., 2017; Tavakoli et al., 2018). In this work, we investigated the hysteresis behavior of the devices with and without SWCNTs and the results have been plotted in Figures 8A, 8B, and S9. On the basis of the measured hysteresis index, the addition of SWCNTs into the TiO_2 remarkably reduced the hysteresis effect as compared with the TiO_2-only device, which is in good agreement with our previous finding (Batmunkh et al., 2017b). However, no considerable differences can be noted among the different CNTs-based

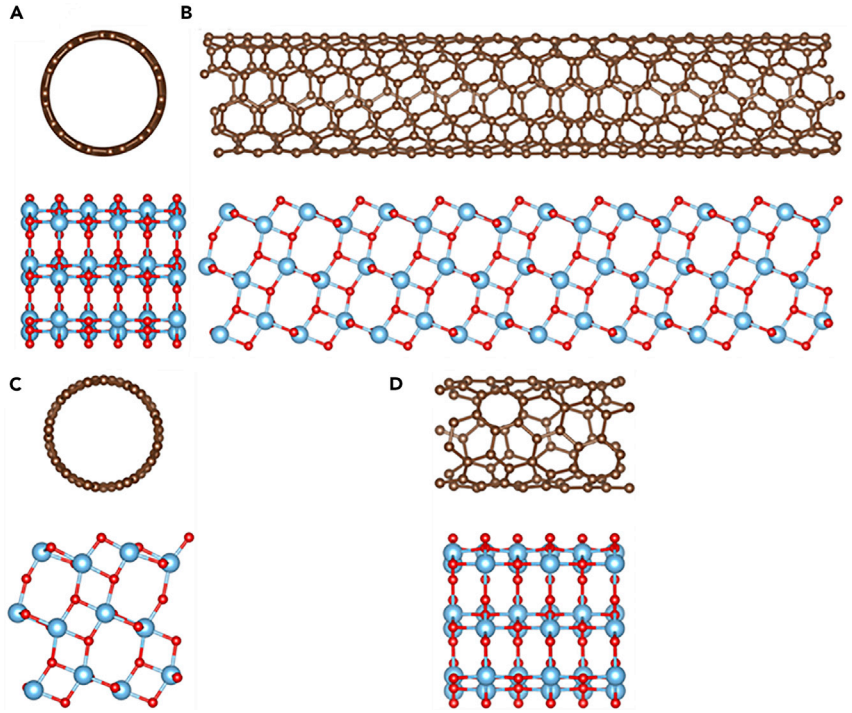

Figure 6. Density Functional Theory Calculations of the TiO_2 with Isolated Nanotubes

The (A) front and (B) side view of the interface between the (6,5) CNT and the TiO_2(101) surface, and the (C) front and (D) side view of the interface between the (6,3) CNT and the TiO_2(101) surface. Brown spheres are for the C atoms, red spheres are for the O atoms, and blue spheres are for the Ti atoms.

devices (see Figure S9). We attribute the low hysteresis in our devices to the enhanced charge transport at the ETL/perovskite interface, which may have helped to balance the electron and hole transport within the PSCs.

In addition to the hysteresis behavior, the stability of the fabricated PSCs under continuous light illumination was also studied. The un-encapsulated devices were exposed to prolonged illumination conditions (100 mW cm^{-2}) over 60 min in an ambient environment, and the *J-V* curves were acquired in the reverse scan direction every 5 min. The normalized PV parameters are illustrated in Figures 8C and S10. Except in the TiO_2/s-SWCNTs-based device, improvement in the stability of the SWCNTs-based devices can be observed as compared with the TiO_2-only device. The rapid performance degradation for the TiO_2/s-SWCNTs-based PSC may be attributed to the lower stability of s-SWCNTs under ambient conditions as compared with their m-SWCNTs counterpart (Tey et al., 2012). It has been established that the constant DOS near the Fermi level (EF) of m-SWCNTs resulting from the lack states close to the (EF) makes the m-SWCNTs less sensitive to the surrounding environment. In contrast, s-SWCNT species exhibit many states much closer to the EF and hence the DOS shift has a more pronounced effect leading to a variation in the carrier concentration upon exposure to ambient environment. We speculate that the presence of m-SWCNTs can effectively suppress the degradation rate owing to their lower sensitivity to the surrounding environment. Generally, the main factor in the decrease of the PCEs of our PSC devices was the FF value. Surprisingly, all the m-SWCNTs-containing devices showed either a negligible decrease in the J_{sc} (e.g., TiO_2/1:1 s-:m-SWCNTs PSC retained 99.97% of its initial J_{oc} after 60 min of light exposure) or even an improved J_{sc} (e.g., TiO_2/2:1 s-:m-SWCNTs and TiO_2/1:2 s-:m-SWCNTs PSCs exhibited improved J_{sc} of 0.4% and 1.9% of their initial J_{sc}, respectively). These results shed light on the importance of the electrical behavior of SWCNTs incorporated not only on the device performances but also on the hysteresis and stability of the devices.

In general, PSCs show severe degradation in their performance upon exposure to humidity, heat, and light (Shin et al., 2017; Luo et al., 2017a). One of the proposed mechanisms behind the PSC degradation by light

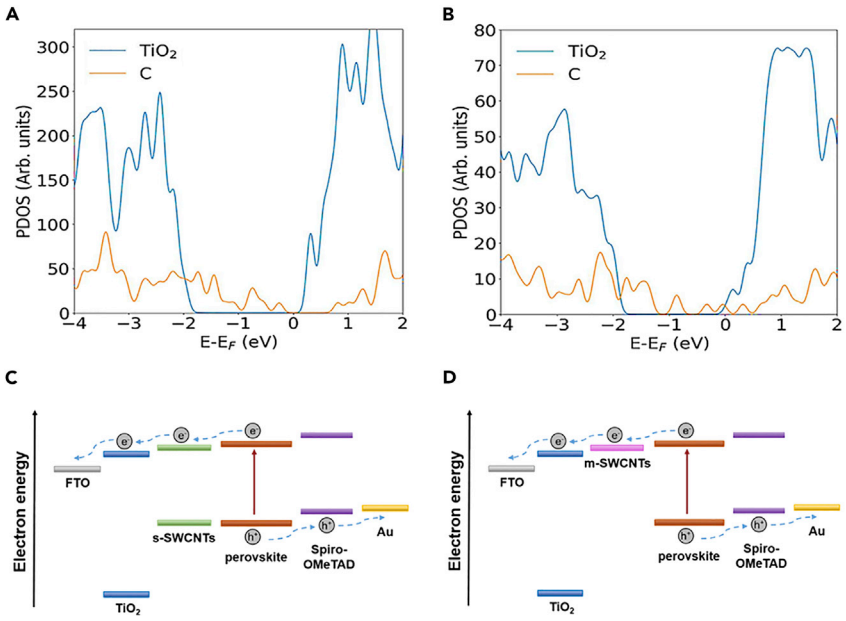

Figure 7. Energy Band Alignments of the Solar Cells Fabricated with Different Types of SWCNTs

The partial density of states (PDOS) for (A) the (6,5) CNT-TiO_2 (101) system and (B) the (6,3) CNT-TiO_2 (101) system. Energy band diagram of PSCs with incorporated (C) s-SWCNTs and (D) m-SWCNTs.

is the light-induced desorption of surface-adsorbed oxygen (Leijtens et al., 2013). Such a process is believed to increase the number of deep electron trap sites leading to the recombination of the trapped electrons with the holes in the perovskite or HTM. In this regard, SWCNTs may play an important role in passivating those TiO_2 trap sites, which can improve the stability of the devices during prolonged operation. In addition, the high oxygen adsorption ability of SWCNTs may have reduced degradation hence improving device stability. As for the heat, the high thermal conductivity of SWCNTs may also help relieve the thermal decomposition of the devices.

Conclusion

In this work, highly enriched semiconducting and metallic SWCNT samples were prepared using a column chromatography method and used in solution-processable ETLs for highly efficient PSCs. The introduction of different SWCNTs families with optimized contents resulted in significant enhancements in the PCEs, considerable reductions in the *J-V* hysteresis of the devices, and improved stabilities when subjected to continuous light illumination. The champion device fabricated with TiO_2/2:1 s-:m-SWCNTs ETL exhibited a remarkable PCE of up to 19.35%. This remarkable performance of the PSC is mainly attributed to the improved electron conductivity and effective electron extraction due to the better band energy alignment at the ELT/perovskite interface. We anticipate that this study will make an important contribution in designing SWCNTs-based photoelectrodes for high-performing PSCs.

Limitations of the Study

In this study, the effect of the exact electrical properties of SWCNTs on the device performance and charge carrier dynamics is investigated. Although commercial SWCNTs were sorted into semiconducting and metallic nanotubes, the semiconducting and metallic nanotube fractions are still a mixture of a large number of chirality species with different electrical behavior, diameters, and energy band gaps. It is anticipated that, by employing chirality-controlled SWCNTs, the charge collection and transport processes can be further improved. The energy levels of the ETLs should be further scrutinized after the introduction of different SWCNT families by UV photoelectron spectroscopy to provide an insight into the interfacial band alignment between the ETL and the perovskite layer. Finally, a more complete range of ratios of semiconducting to metallic nanotubes can be further studied, which may lead to a better understanding of the

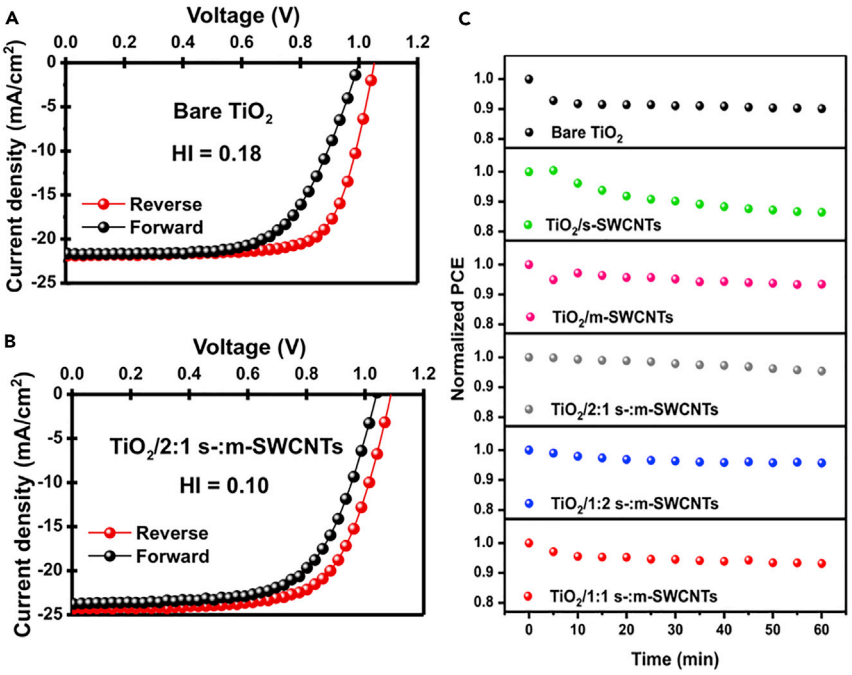

Figure 8. Device Stability and Hysteresis Assessment

(A and B) *J-V* curves measured at forward scan and reverse scan for the devices fabricated with (A) TiO_2-only and (B) TiO_2/2:1 s-:m-SWCNTs. The hysteresis behavior of the devices was evaluated through the hysteresis index (HI) shown in the plots, which was calculated as reported previously (Jiang et al., 2017).

(C) Normalized PCE of the PSCs showing their degradation rate during the first 60 min of operation.

interaction and charge transfer mechanisms between the nanotubes themselves and the nanotubes with the TiO_2.

METHODS

All methods can be found in the accompanying Transparent Methods supplemental file.

SUPPLEMENTAL INFORMATION

Supplemental Information can be found online at https://doi.org/10.1016/j.isci.2019.03.015.

ACKNOWLEDGMENTS

We acknowledge the use of South Australian nodes of the Australian Microscopy & Microanalysis Research Facility (AMMRF) and Australian National Fabrication Facility (ANFF) at Flinders University and the University of Queensland. A.S.R.B. acknowledges Saudi Arabian Cultural Mission (SACM) and the Ministry of Education of Saudi Arabia for their financial support during his study in Australia. The support of the Australian Research Council Discovery Program (DP160101301) is gratefully acknowledged.

AUTHOR CONTRIBUTIONS

A.S.R.B., M.B., and J.G.S. conceived the project and designed the experiments. A.S.R.B. fabricated the devices, analyzed the data, and wrote the initial draft. L.Y. and M.B. contributed to the experimental work. S.A.T. and M.J.S.S. carried out the computational studies. P.E.S. conducted the TRPL measurements. All authors commented on the manuscript. J.G.S. supervised the project.

DECLARATION OF INTERESTS

The authors declare no competing interests.

Received: January 1, 2019
Revised: February 25, 2019
Accepted: March 15, 2019
Published: April 26, 2019

REFERENCES

Agresti, A., Pescetelli, S., Cinà, L., Konios, D., Kakavelakis, G., Kymakis, E., and Carlo, A.D. (2016). Efficiency and stability enhancement in perovskite solar cells by inserting lithium-neutralized graphene oxide as electron transporting layer. Adv. Funct. Mater. *26*, 2686–2694.

Aitola, K., Sveinbjörnsson, K., Correa-Baena, J.-P., Kaskela, A., Abate, A., Tian, Y., Johansson, E.M., Grätzel, M., Kauppinen, E.I., and Hagfeldt, A. (2016). Carbon nanotube-based hybrid hole-transporting material and selective contact for high efficiency perovskite solar cells. Energy Environ. Sci. *9*, 461–466.

Ao, G., Khripin, C.Y., and Zheng, M. (2014). DNA-controlled partition of carbon nanotubes in polymer aqueous two-phase systems. J. Am. Chem. Soc. *136*, 10383–10392.

Bai, Y., Mora-Sero, I., De Angelis, F., Bisquert, J., and Wang, P. (2014). Titanium dioxide nanomaterials for photovoltaic applications. Chem. Rev. *114*, 10095–10130.

Ball, J.M., Lee, M.M., Hey, A., and Snaith, H.J. (2013). Low-temperature processed meso-superstructured to thin-film perovskite solar cells. Energy Environ. Sci. *6*, 1739–1743.

Bati, A.S.R., Yu, L., Batmunkh, M., and Shapter, J.G. (2018). Synthesis, purification, properties and characterization of sorted single-walled carbon nanotubes. Nanoscale *10*, 22087–22139.

Batmunkh, M., Macdonald, T.J., Shearer, C.J., Bat-Erdene, M., Wang, Y., Biggs, M.J., Parkin, I.P., Nann, T., and Shapter, J.G. (2017a). Carbon nanotubes in TiO2 nanofiber photoelectrodes for high-performance perovskite solar cells. Adv. Sci. (Weinh) *4*, 1600504.

Batmunkh, M., Shearer, C.J., Bat-Erdene, M., Biggs, M.J., and Shapter, J.G. (2017b). Single-walled carbon nanotubes enhance the efficiency and stability of mesoscopic perovskite solar cells. ACS Appl. Mater. Interfaces *9*, 19945–19954.

Batmunkh, M., Shearer, C.J., Biggs, M.J., and Shapter, J.G. (2015). Nanocarbons for mesoscopic perovskite solar cells. J. Mater. Chem. A *3*, 9020–9031.

Blackburn, J.L., Barnes, T.M., Beard, M.C., Kim, Y.-H., Tenent, R.C., Mcdonald, T.J., To, B., Coutts, T.J., and Heben, M.J. (2008). Transparent conductive single-walled carbon nanotube networks with precisely tunable ratios of semiconducting and metallic nanotubes. ACS Nano *2*, 1266–1274.

Cai, M., Wu, Y., Chen, H., Yang, X., Qiang, Y., and Han, L. (2017). Cost-performance analysis of perovskite solar modules. Adv. Sci. (Weinh) *4*, 1600269.

Chen, B., Yang, M., Priya, S., and Zhu, K. (2016). Origin of J–V hysteresis in perovskite solar cells. J. Phys. Chem. Lett. *7*, 905–917.

Dang, X., Yi, H., Ham, M.-H., Qi, J., Yun, D.S., Ladewski, R., Strano, M.S., Hammond, P.T., and Belcher, A.M. (2011). Virus-templated self-assembled single-walled carbon nanotubes for highly efficient electron collection in photovoltaic devices. Nat. Nanotechnol. *6*, 377–384.

Edri, E., Kirmayer, S., Henning, A., Mukhopadhyay, S., Gartsman, K., Rosenwaks, Y., Hodes, G., and Cahen, D. (2014). Why lead methylammonium tri-iodide perovskite-based solar cells require a mesoporous electron transporting scaffold (but not necessarily a hole conductor). Nano Lett. *14*, 1000–1004.

Green, M.A., Ho-Baillie, A., and Snaith, H.J. (2014). The emergence of perovskite solar cells. Nat. Photonics *8*, 506–514.

Habisreutinger, S.N., Leijtens, T., Eperon, G.E., Stranks, S.D., Nicholas, R.J., and Snaith, H.J. (2014a). Carbon nanotube/polymer composites as a highly stable hole collection layer in perovskite solar cells. Nano Lett. *14*, 5561–5568.

Habisreutinger, S.N., Leijtens, T., Eperon, G.E., Stranks, S.D., Nicholas, R.J., and Snaith, H.J. (2014b). Enhanced hole extraction in perovskite solar cells through carbon nanotubes. J. Phys. Chem. Lett. *5*, 4207–4212.

Habisreutinger, S.N., Nicholas, R.J., and Snaith, H.J. (2017). Carbon nanotubes in perovskite solar cells. Adv. Energy Mater. *7*, 1601839.

Han, G.S., Song, Y.H., Jin, Y.U., Lee, J.-W., Park, N.-G., Kang, B.K., Lee, J.-K., Cho, I.S., Yoon, D.H., and Jung, H.S. (2015). Reduced graphene oxide/mesoporous TiO2 nanocomposite based perovskite solar cells. ACS Appl. Mater. Interfaces *7*, 23521–23526.

He, M., Zheng, D., Wang, M., Lin, C., and Lin, Z. (2014). High efficiency perovskite solar cells: from complex nanostructure to planar heterojunction. J. Mater. Chem. A *2*, 5994–6003.

Hendriks, K.H., Van Franeker, J.J., Bruijnaers, B.J., Anta, J.A., Wienk, M.M., and Janssen, R.A. (2017). 2-Methoxyethanol as a new solvent for processing methylammonium lead halide perovskite solar cells. J. Mater. Chem. A *5*, 2346–2354.

Hou, Q., Ren, J., Chen, H., Yang, P., Shao, Q., Zhao, M., Zhao, X., He, H., Wang, N., and Luo, Q. (2018). Synergistic hematite-fullerene electron-extracting layers for improved efficiency and stability in perovskite solar cells. ChemElectroChem *5*, 726–731.

Hu, W., Liu, T., Yin, X., Liu, H., Zhao, X., Luo, S., Guo, Y., Yao, Z., Wang, J., and Wang, N. (2017). Hematite electron-transporting layers for environmentally stable planar perovskite solar cells with enhanced energy conversion and lower hysteresis. J. Mater. Chem. A *5*, 1434–1441.

Ihly, R., Dowgiallo, A.-M., Yang, M., Schulz, P., Stanton, N.J., Reid, O.G., Ferguson, A.J., Zhu, K., Berry, J.J., and Blackburn, J.L. (2016). Efficient charge extraction and slow recombination in organic–inorganic perovskites capped with semiconducting single-walled carbon nanotubes. Energy Environ. Sci. *9*, 1439–1449.

Jeon, I., Chiba, T., Delacou, C., Guo, Y., Kaskela, A., Reynaud, O., Kauppinen, E.I., Maruyama, S., and Matsuo, Y. (2015). Single-walled carbon nanotube film as electrode in indium-free planar heterojunction perovskite solar cells: investigation of electron-blocking layers and dopants. Nano Lett. *15*, 6665–6671.

Jeon, N.J., Noh, J.H., Kim, Y.C., Yang, W.S., Ryu, S., and Seok, S.I. (2014). Solvent engineering for high-performance inorganic–organic hybrid perovskite solar cells. Nat. Mater. *13*, 897.

Jiang, Q., Chu, Z., Wang, P., Yang, X., Liu, H., Wang, Y., Yin, Z., Wu, J., Zhang, X., and You, J. (2017). Planar-structure perovskite solar cells with efficiency beyond 21%. Adv. Mater. (Weinh) *29*, 1703852.

Jorio, A., Pimenta, M., Souza Filho, A., Saito, R., Dresselhaus, G., and Dresselhaus, M. (2003). Characterizing carbon nanotube samples with resonance Raman scattering. New J. Phys. *5*, 139.

Ke, W., Fang, G., Liu, Q., Xiong, L., Qin, P., Tao, H., Wang, J., Lei, H., Li, B., and Wan, J. (2015). Low-temperature solution-processed tin oxide as an alternative electron transporting layer for efficient perovskite solar cells. J. Am. Chem. Soc. *137*, 6730–6733.

Ke, W., Stoumpos, C.C., Logsdon, J.L., Wasielewski, M.R., Yan, Y., Fang, G., and Kanatzidis, M.G. (2016). TiO2–ZnS cascade electron transport layer for efficient formamidinium tin iodide perovskite solar cells. J. Am. Chem. Soc. *138*, 14998–15003.

Kim, H.-S., Im, S.H., and Park, N.-G. (2014). Organolead halide perovskite: new horizons in solar cell research. J. Phys. Chem. C *118*, 5615–5625.

Kim, H., Lim, K.-G., and Lee, T.-W. (2016). Planar heterojunction organometal halide perovskite solar cells: roles of interfacial layers. Energy Environ. Sci. *9*, 12–30.

Kim, Y.J., Lee, M.H., Kim, H.J., Lim, G., Choi, Y.S., Park, N.G., Kim, K., and Lee, W.I. (2009). Formation of highly efficient dye-sensitized solar cells by hierarchical pore generation with nanoporous TiO2 spheres. Adv. Mater. *21*, 3668–3673.

Leijtens, T., Eperon, G.E., Pathak, S., Abate, A., Lee, M.M., and Snaith, H.J. (2013). Overcoming ultraviolet light instability of sensitized TiO 2 with

meso-superstructured organometal tri-halide perovskite solar cells. Nat. Commun. *4*, 2885.

Li, H., Cao, K., Cui, J., Liu, S., Qiao, X., Shen, Y., and Wang, M. (2016). 14.7% efficient mesoscopic perovskite solar cells using single walled carbon nanotubes/carbon composite counter electrodes. Nanoscale *8*, 6379–6385.

Li, Z., Kulkarni, S.A., Boix, P.P., Shi, E., Cao, A., Fu, K., Batabyal, S.K., Zhang, J., Xiong, Q., and Wong, L.H. (2014). Laminated carbon nanotube networks for metal electrode-free efficient perovskite solar cells. ACS Nano *8*, 6797–6804.

Long, R. (2013). Electronic structure of semiconducting and metallic tubes in TiO2/carbon nanotube heterojunctions: density functional theory calculations. J. Phys. Chem. Lett. *4*, 1340–1346.

Luo, Q., Chen, H., Lin, Y., Du, H., Hou, Q., Hao, F., Wang, N., Guo, Z., and Huang, J. (2017a). Discrete iron (III) oxide nanoislands for efficient and photostable perovskite solar cells. Adv. Funct. Mater. *27*, 1702090.

Luo, Q., Ma, H., Hao, F., Hou, Q., Ren, J., Wu, L., Yao, Z., Zhou, Y., Wang, N., and Jiang, K. (2017b). Carbon nanotube based inverted flexible perovskite solar cells with all-inorganic charge contacts. Adv. Funct. Mater. *27*, 1703068.

Luo, Q., Ma, H., Hou, Q., Li, Y., Ren, J., Dai, X., Yao, Z., Zhou, Y., Xiang, L., and Du, H. (2018). All-carbon-electrode-based endurable flexible perovskite solar cells. Adv. Funct. Mater. *28*, 1706777.

Macdonald, T.J., Tune, D.D., Dewi, M.R., Gibson, C.T., Shapter, J.G., and Nann, T. (2015). A TiO2 nanofiber–carbon nanotube-composite photoanode for improved efficiency in dye-sensitized solar cells. ChemSusChem *8*, 3396–3400.

McEuen, P.L., and Park, J.-Y. (2004). Electron transport in single-walled carbon nanotubes. MRS Bull. *29*, 272–275.

Nakata, K., and Fujishima, A. (2012). TiO2 photocatalysis: Design and applications. J. Photochem. Photobiol. C *13*, 169–189.

National Renewable Energy Laboratory. (2019). Best research-cell efficiencies chart. https://www.nrel.gov/pv/assets/pdfs/best-reserch-cell-efficiencies.pdf.

Ohsaka, T., Izumi, F., and Fujiki, Y. (1978). Raman spectrum of anatase, TiO2. J. Raman Spectrosc. *7*, 321–324.

Park, N.-G. (2013). Organometal perovskite light absorbers toward a 20% efficiency low-cost solid-state mesoscopic solar cell. J. Phys. Chem. Lett. *4*, 2423–2429.

Peng, J., Wu, Y., Ye, W., Jacobs, D.A., Shen, H., Fu, X., Wan, Y., Wu, N., Barugkin, C., and Nguyen, H.T. (2017). Interface passivation using ultrathin polymer–fullerene films for high-efficiency perovskite solar cells with negligible hysteresis. Energy Environ. Sci. *10*, 1792–1800.

Petrus, M.L., Schlipf, J., Li, C., Gujar, T.P., Giesbrecht, N., Müller-Buschbaum, P., Thelakkat, M., Bein, T., Hüttner, S., and Docampo, P. (2017). Capturing the Sun: a review of the challenges and perspectives of perovskite solar cells. Adv. Energy Mater. *7*, 1700264.

Qian, D., Wagner, G.J., Liu, W.K., Yu, M.-F., and Ruoff, R.S. (2002). Mechanics of carbon nanotubes. Appl. Mech. Rev. *55*, 495–533.

Sadollahkhani, A., Liu, P., Leandri, V., Safdari, M., Zhang, W., and Gardner, J.M. (2017). Energetic barriers to interfacial charge transfer and ion movement in perovskite solar cells. ChemPhysChem *18*, 3047–3055.

Shin, S.S., Yeom, E.J., Yang, W.S., Hur, S., Kim, M.G., Im, J., Seo, J., Noh, J.H., and Seok, S.I. (2017). Colloidally prepared La-doped BaSnO3 electrodes for efficient, photostable perovskite solar cells. Science *356*, 167–171.

Singh, P., Campidelli, S., Giordani, S., Bonifazi, D., Bianco, A., and Prato, M. (2009). Organic functionalisation and characterisation of single-walled carbon nanotubes. Chem. Soc. Rev. *38*, 2214–2230.

Tanaka, T., Urabe, Y., Nishide, D., and Kataura, H. (2009). Continuous separation of metallic and semiconducting carbon nanotubes using agarose gel. Appl. Phys. Express *2*, 125002.

Tavakoli, M.M., Yadav, P., Tavakoli, R., and Kong, J. (2018). Surface engineering of TiO2 ETL for highly efficient and hysteresis-less planar perovskite solar cell (21.4%) with enhanced open-circuit voltage and stability. Adv. Energy Mater. *8*, 1800794.

Tey, J.N., Ho, X., and Wei, J. (2012). Effect of doping on single-walled carbon nanotubes network of different metallicity. Nanoscale Res. Lett. *7*, 548.

Wang, J.T.-W., Ball, J.M., Barea, E.M., Abate, A., Alexander-Webber, J.A., Huang, J., Saliba, M., Mora-Sero, I., Bisquert, J., and Snaith, H.J. (2013). Low-temperature processed electron collection layers of graphene/TiO2 nanocomposites in thin film perovskite solar cells. Nano Lett. *14*, 724–730.

Wang, K., Liu, C., Du, P., Zheng, J., and Gong, X. (2015). Bulk heterojunction perovskite hybrid solar cells with large fill factor. Energy Environ. Sci. *8*, 1245–1255.

Wetzelaer, G.J.A., Scheepers, M., Sempere, A.M., Momblona, C., Ávila, J., and Bolink, H.J. (2015). Trap-assisted non-radiative recombination in organic–inorganic perovskite solar cells. Adv. Mater. *27*, 1837–1841.

Woan, K., Pyrgiotakis, G., and Sigmund, W. (2009). Photocatalytic carbon-nanotube–TiO2 composites. Adv. Mater. *21*, 2233–2239.

Wojciechowski, K., Stranks, S.D., Abate, A., Sadoughi, G., Sadhanala, A., Kopidakis, N., Rumbles, G., Li, C.-Z., Friend, R.H., and Jen, A.K.-Y. (2014). Heterojunction modification for highly efficient organic–inorganic perovskite solar cells. ACS Nano *8*, 12701–12709.

Yoon, H., Kang, S.M., Lee, J.-K., and Choi, M. (2016). Hysteresis-free low-temperature-processed planar perovskite solar cells with 19.1% efficiency. Energy Environ. Sci. *9*, 2262–2266.

Yu, J.C., Hong, J.A., Jung, E.D., Kim, D.B., Baek, S.-M., Lee, S., Cho, S., Park, S.S., Choi, K.J., and Song, M.H. (2018). Highly efficient and stable inverted perovskite solar cell employing PEDOT:GO composite layer as a hole transport layer. Sci. Rep. *8*, 1070.

Zhou, W., Bai, X., Wang, E., and Xie, S. (2009). Synthesis, structure, and properties of single-walled carbon nanotubes. Adv. Mater. *21*, 4565–4583.

Zhu, Y., Deng, K., Sun, H., Gu, B., Lu, H., Cao, F., Xiong, J., and Li, L. (2018). TiO2 phase junction electron transport layer boosts efficiency of planar perovskite solar cells. Adv. Sci. *5*, 1700614.

ISCI, Volume *14*

Supplemental Information

Electrically Sorted Single-Walled Carbon Nanotubes-Based Electron Transporting Layers for Perovskite Solar Cells

Abdulaziz S.R. Bati, LePing Yu, Sherif Abdulkader Tawfik, Michelle J.S. Spencer, Paul E. Shaw, Munkhbayar Batmunkh, and Joseph G. Shapter

Transparent Methods

Materials

Unless otherwise stated, all chemicals were purchased from Sigma-Aldrich. Unsorted SWCNTs (Raw HiPCO, diameter 0.8–1.2 nm, length 100–1,000 nm) were purchased from Nanointegris. Alkyl dextran-based gel beads in ethanol (Sephacryl S-200 HR) were purchased from GE Healthcare. Fluorine-doped tin oxide (FTO) coated glass substrates were purchased from Xin Yan Technology LTD. Mesoporous titania paste (30 NR-D), formamidinium iodide (FAI), methylamine bromide (MABr) and tris(1-(pyridin-2-yl)-1H-pyrazol)cobalt(III) tris(hexafluorophosphate) (FK102 Co(III)PF6) salt were purchased from Greatcell Solar. Lead iodide (PbI_2) and lead bromide ($PbBr_2$) (99%) were purchased from Tokyo Chemical Industry (TCI). 2,2′,7,7′-Tetrakis(N,N-di-pmethoxyphenylamine)-9,9′-spirobifluorene (Spiro-OMeTAD) was purchased from Merck.

SWCNTs Dispersion

The as-produced SWCNTs were dispersed in an aqueous solution of 0.5 wt% sodium dodecyl sulfate (SDS) at a concentration of 1 mg/mL using a tip ultrasonication (Sonics VCX 750W) with 6.5 mm Ti microtip for 45 min at 25 % of maximum amplitude. The samples were immersed in an ice-cold water bath during sonication to prevent heating. After sonication, fixed-angle centrifugation (Beckman equipped with a Type 70 Ti rotor) was carried out at high speed of 41200 rpm for 45 min to remove the bundles and impurities. The top 80% of the supernatant was collected using a pipette for further use.

Separation of Semiconducting and Metallic SWCNTs

Stock solutions of 0.5 wt% SDS, 1 wt% SDS, and 1 wt% sodium deoxycholate (DOC) were first prepared. Approximately 30 mL gel was added to the separation column. After the column was equilibrated with 0.5% SDS, 10 mL of the centrifuged solution was loaded into the column. By adding 0.5% SDS solution to the column, unbound metallic nanotubes were collected. In order to ensure that all metallic nanotubes were eluted, 1% SDS solution was further loaded into the column. Finally, 1% DOC was added to the column to collect the s-SWCNTs.

Preparation of TiO_2 NPs-SWCNTs Nanocomposites

The TiO_2 paste was diluted in ethanol (1:6 w/w). The various TiO_2 NPs-SWCNTs nanocomposites were prepared by adding an appropriate volume of each SWCNTs solution to the diluted TiO_2 dispersion. The concentration of SWCNTs in the nanocomposite was controlled by changing the volume of SWCNT solution.

Device fabrication

The FTO substrates were cleaned with a detergent (Pyroneg), distilled water, acetone and ethanol in turn for 10 min each using ultrasonication. A TiO_2 compact layer was spin coated onto the FTO at 3000 rpm for 45 s (repeated twice) from a precursor solution containing 0.1 M titanium diisopropoxide bis(acetylacetonate) (75 wt % in isopropanol) in 1-butanol solution. Each spin-coating process involved thermal annealing at 150 °C for 15 min. Mesoporous TiO_2 solution was deposited onto the compact layer at a speed of 4000 rpm for 20 s followed by annealing at 450 °C for 1 h in air. After cooling down to room temperature, the films were immersed in a 20 mM $TiCl_4$ aqueous for 20 min at 90 °C, followed by further annealing for 1 h at 450 °C. The substrates were subsequently transferred into a nitrogen-filled glove box.

The mixed-cation lead mixed-halide perovskite solution was prepared as described previously. FAI (1 M), PbI_2 (1.1 M), MABr (0.2 M) and $PbBr_2$ (0.2 M) were mixed in anhydrous DMF: DMSO 4:1 (v:v). Then, 1.5 M stock solution of CsI in DMSO was added to the perovskite precursor to achieve the triple cation composition. The resulting solution was stirred at 65 °C for 2 h, and subsequently filtered before being spin coated onto the photoelectrodes. The deposition was carried out through a two-step procedure. (i) 1000 rpm for 10 s with a ramp of 250 rpm s^{-1} (ii) 5000 rpm for 30 s with a ramp of 2000 rpm s^{-1}. 100 µL of anhydrous chlorobenzene was gently dropped on the center of spinning substrate ~10 s before the end of the second spin-coating step. The perovskite films were then annealed at 100 °C for 45 min under glovebox conditions.

After the annealing process, the substrates were cooled for few minutes and a hole transporting material (HTM) solution was spin coated at 4000 rpm for 20 s. The HTM solution was prepared by dissolving 57.8 mg spiro-OMeTAD, 23 µL 4-tert-butylpyridine (tBP), 14 µL of bis (trifluoromethylsulphonyl) imide (Li-TFSI) pre-dissolved as a 520 mg/mL in acetonitrile and 16.5 µL of FK102 Co(III) PF6 salt pre-dissolved as a 100 mg/mL in acetonitrile, in 800 µL chlorobenzene. The devices were then left inside a desiccator overnight. Finally, an 50 nm-thick gold top electrode was deposited by thermal evaporator (Angstrom Engineering Covap) under high vacuum at a rate of 1 Å s^{-1}.

Materials Characterization

The optical absorbance spectra were measured using a UV–vis–NIR spectrometer (Perkin Elmer UVvis-NIR Lambda 950) with a wavelength range of 350 to 1350 nm. The cross-sectional images of the devices and the morphology of TiO_2 and/or SWCNTs were obtained with an acceleration voltage of 5 kV using an Inspect F50 SEM (FEI) or a field-emission-scanning electron microscope (JOEL JSM-7001). Raman spectra were acquired using a HORIBA system with the excitation

wavelength of 633 nm, while the spectral mapping were obtained using a Witec Alpha 300RS with a 40× objective and 532 nm laser excitation. Data from transmission electron microscopy (HT7700, TEM) was acquired using 120 kV beam energy.

Photovoltaic Characterization

Photovoltaic measurements were carried out using a Keithley 2400 SMU instrument and recorded using a custom LabView Virtual Instrument program. A 150 W xenon light source (Newport) was used as a light source with an AM 1.5G filter, and a power density of 100 mW cm^{-2} (AM1.5 simulated irradiation) was adjusted using a standard silicon test cell with NIST-traceable certification. The active area of the cells was 0.1 cm^2. The *J*–*V* curves were measured in air in the reverse-scan direction (1.2 to -0.1V). The external quantum efficiency (EQE) spectra were measured by a light source (a xenon lamp) coupled with a monochromator. A calibrated silicon photodiode (Newport) was used as a reference device to calibrate the EQE response. The cells were masked with a non-reflective mask. The scan was taken within the range of 300 nm to 800 nm at an interval of 5 nm. The light stability test was carried out by exposing cells to simulated AM 1.5 (xenon lamp) under ambient conditions. The measurements were obtained via reverse bias scan every 5 min. Electrochemical impedance spectroscopy (EIS) was performed on a full cell configuration using an Autolab PGSTAT128N system at a bias of (0.8 V) under light condition. Fits of the obtained impedance spectra were done using NOVA software with an appropriate equivalent circuit. The time resolved PL were measured with a Fluorolog 3 with time-correlated single photon counting (TCSPC) capability. The excitation source was an LED emitting at 441 nm pulsed at 1 MHz with a pulse width of 1.2 ns and the photoluminescence decays were measured at 767 nm. A longpass filter was used to block any scattered photoexcitation. The instrument response function (IRF) was determined by removing the longpass filter and measuring the

excitation scattered off the sample at 441 nm. The data was fitted with the software application DAS6 (supplied by Jobin−Yvon) using tri-exponential decays convolved with the IRF.

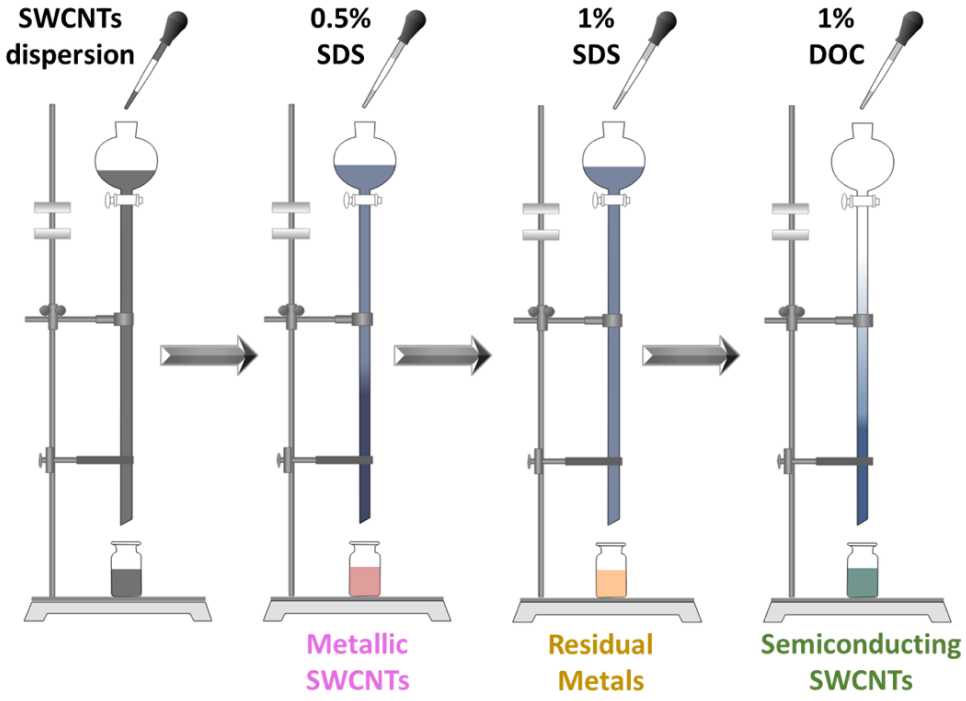

Figure S1. Schematic diagram of the column chromatographic separation method used to produce highly purified semiconducting and metallic nanotubes. Related to Figure 1.

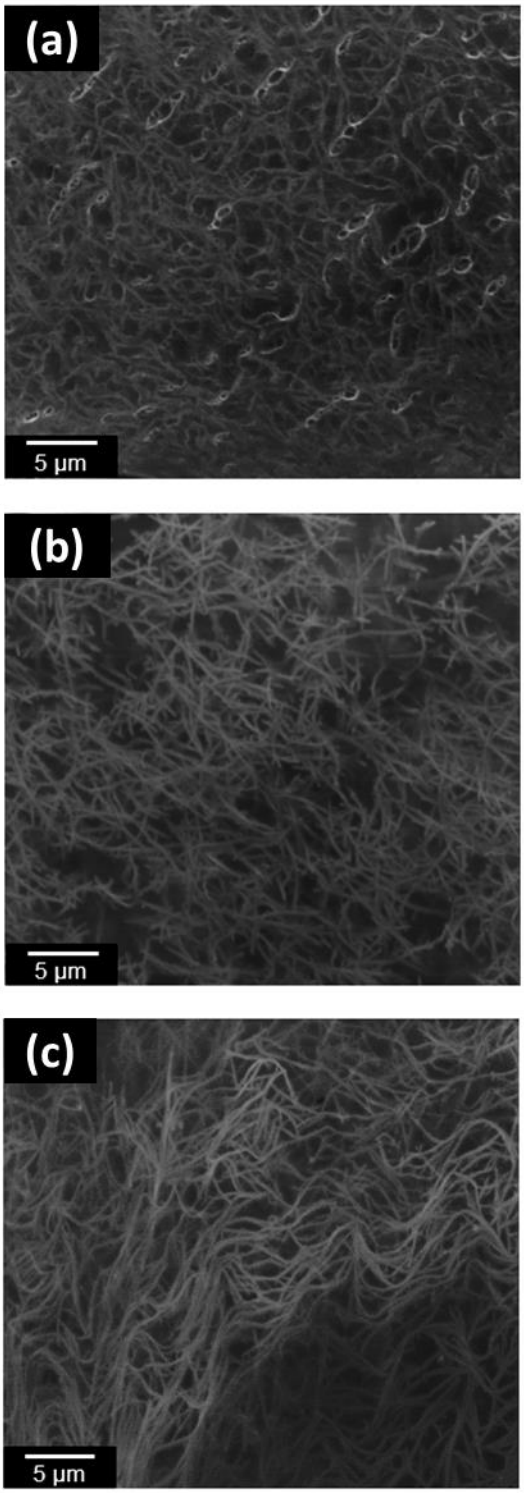

Figure S2. SEM images CNT films formed by (a) p-SWCNTs, (b) s-SWCNTs and (c) m-SWCNTs. Related to Figures 1 and 2.

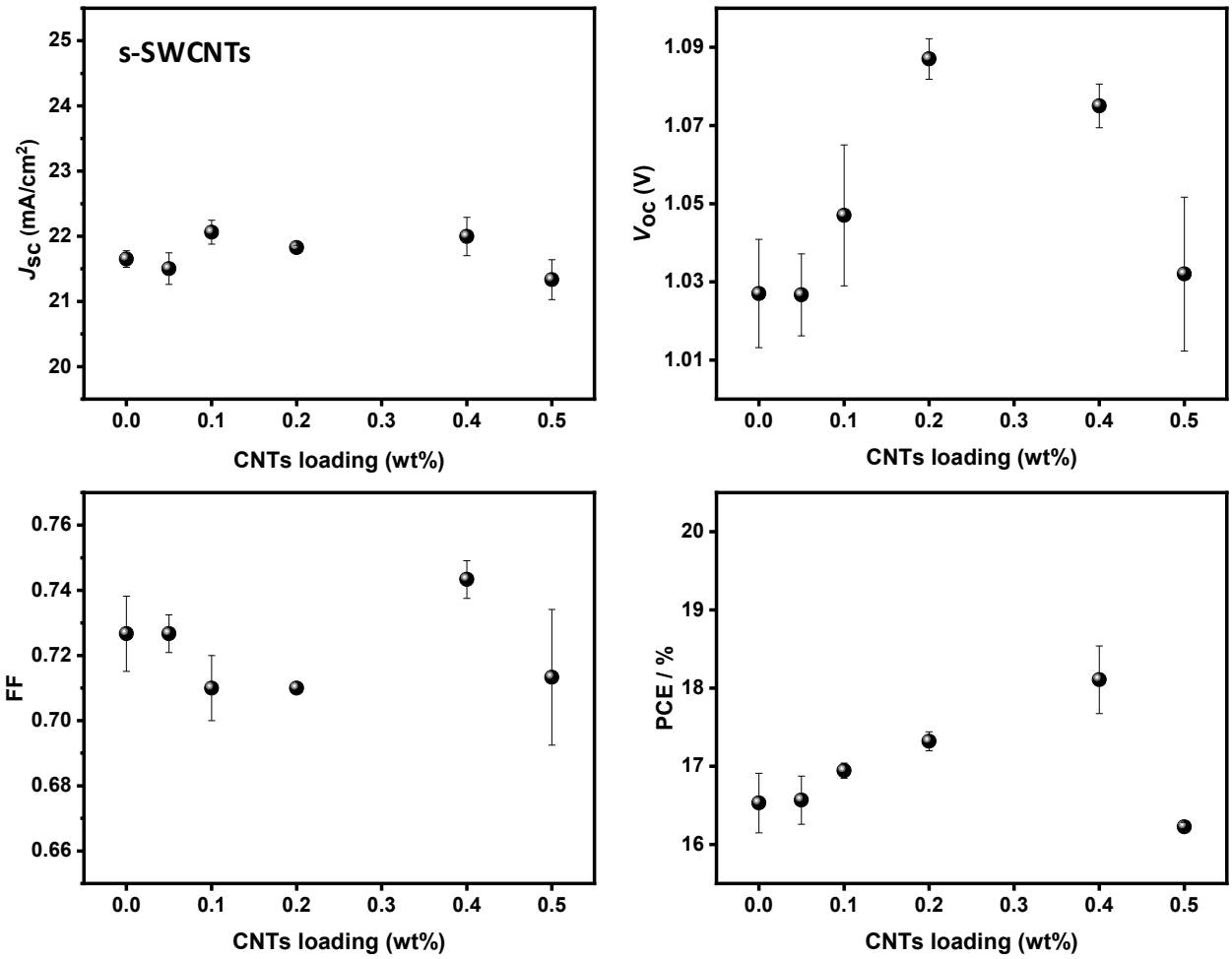

Figure S3. Plots of (a) J_{sc}, (b) V_{oc}, (c) FF, and (d) PCE of the PSCs as a function of s-SWCNT loading in the TiO_2 films. Related to Table 1.

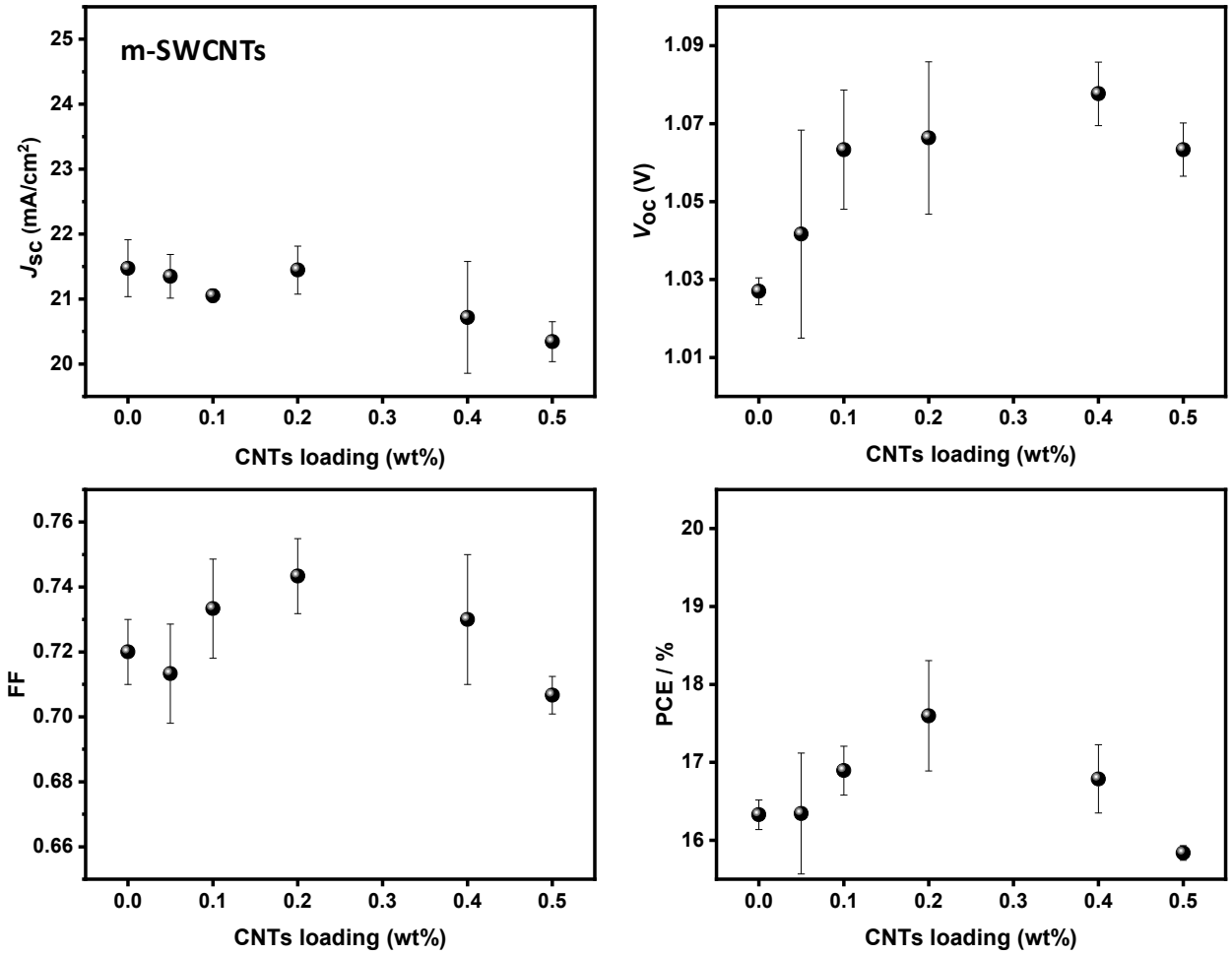

Figure S4. Plots of (a) J_{sc}, (b) V_{oc}, (c) FF, and (d) PCE of the PSCs as a function of m-SWCNT loading in the TiO_2 films. Related to Table 1.

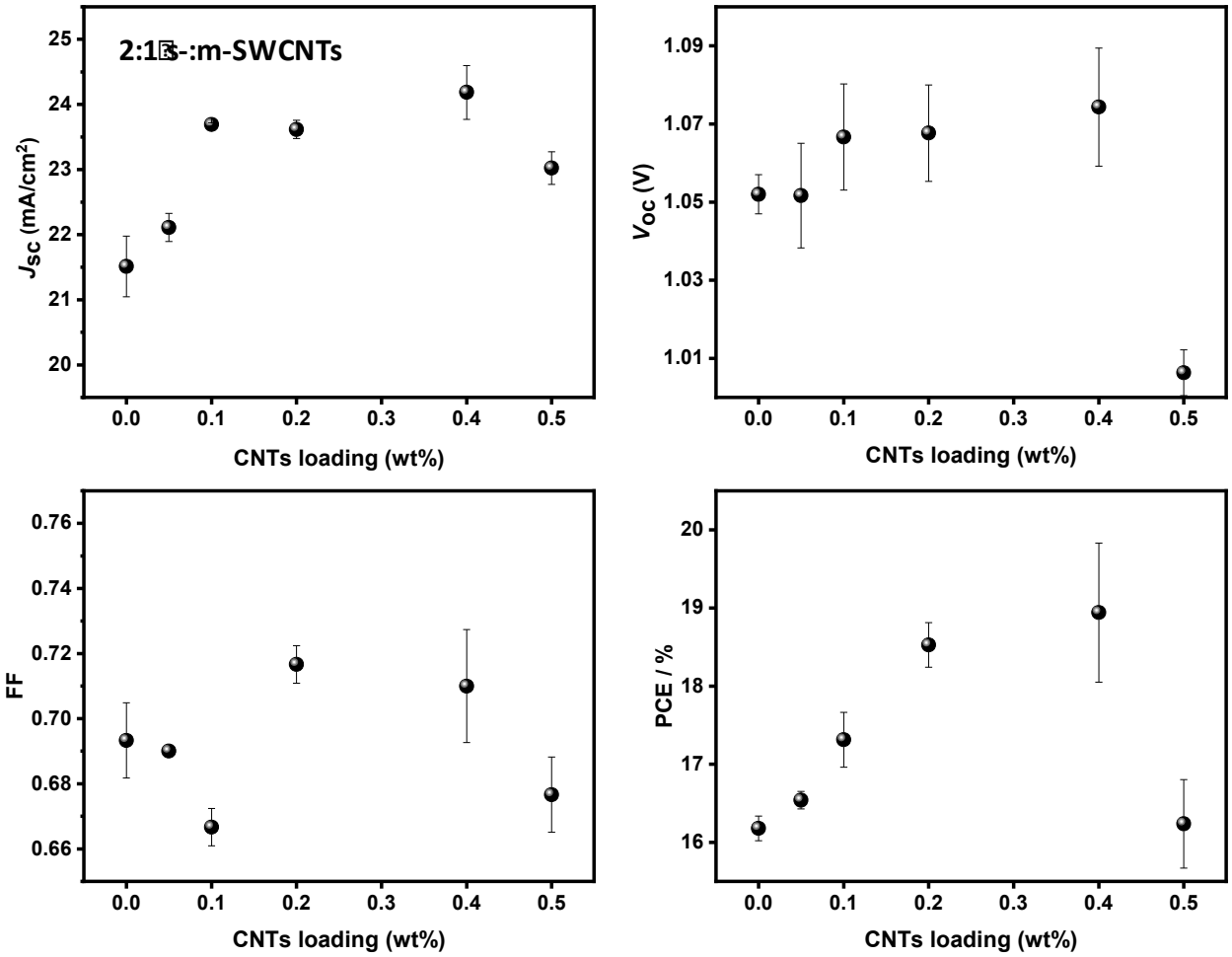

Figure S5. Plots of (a) J_{sc}, (b) V_{oc}, (c) FF, and (d) PCE of the PSCs as a function of 2:1 s-:m-SWCNT loading in the TiO_2 films. Related to Table 1.

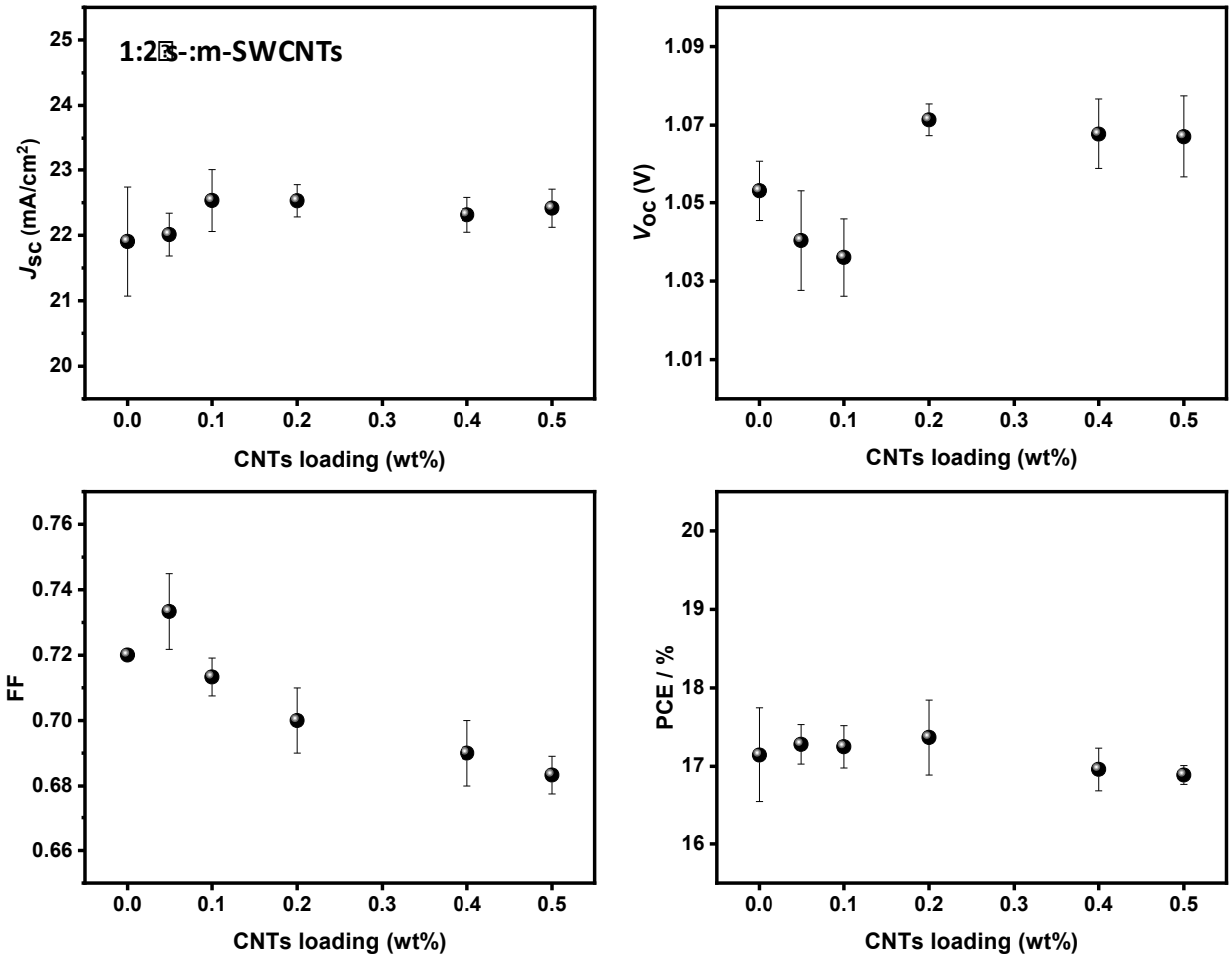

Figure S6. Plots of (a) J_{sc}, (b) V_{oc}, (c) FF, and (d) PCE of the PSCs as a function of 1:2 s-:m-SWCNT concentration in the TiO_2 films. Related to Table 1.

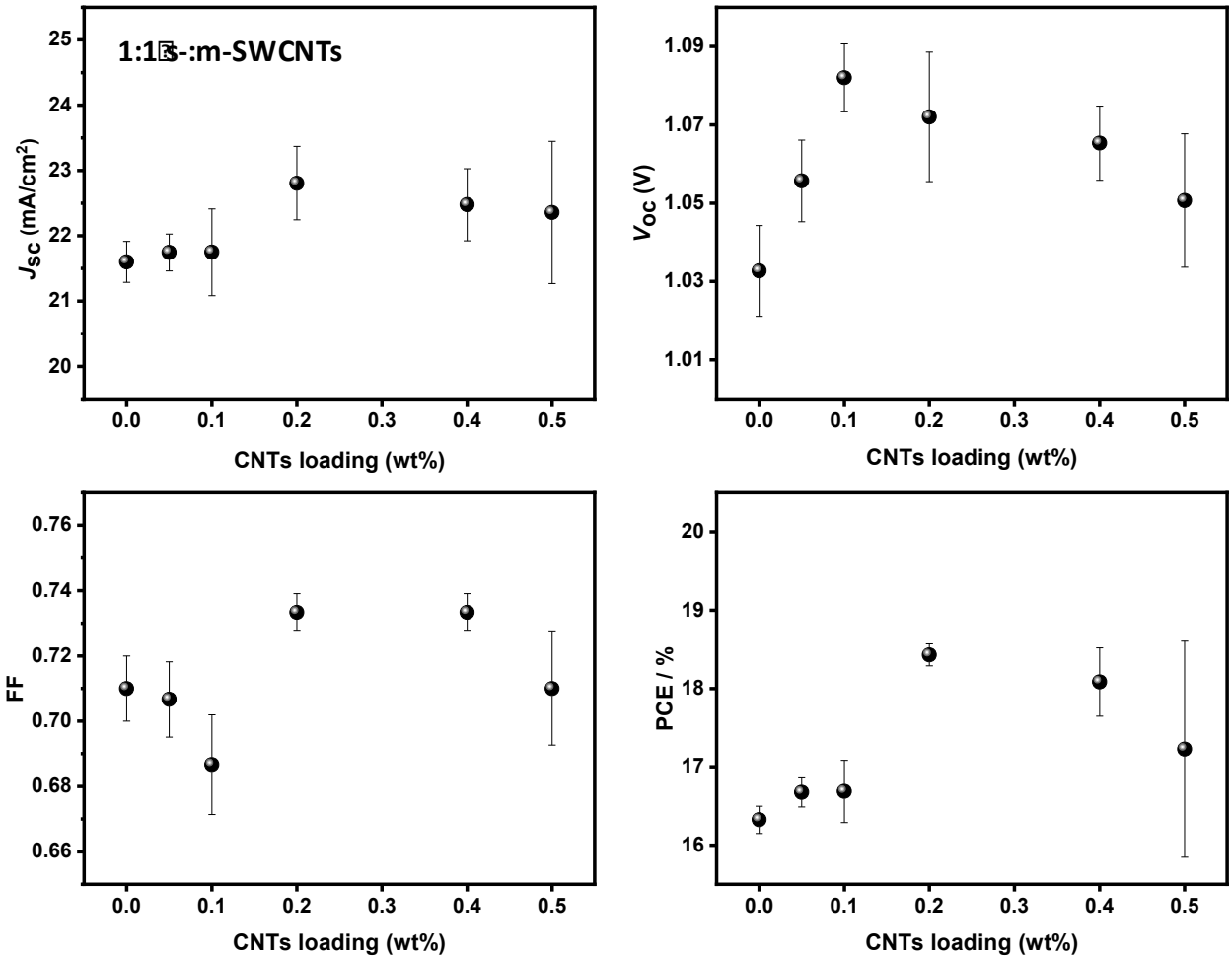

Figure S7. Plots of (a) J_{sc}, (b) V_{oc}, (c) FF, and (d) PCE of the PSCs as a function of 1:1 s-:m-SWCNT loading in the TiO_2 films. Related to Table 1.

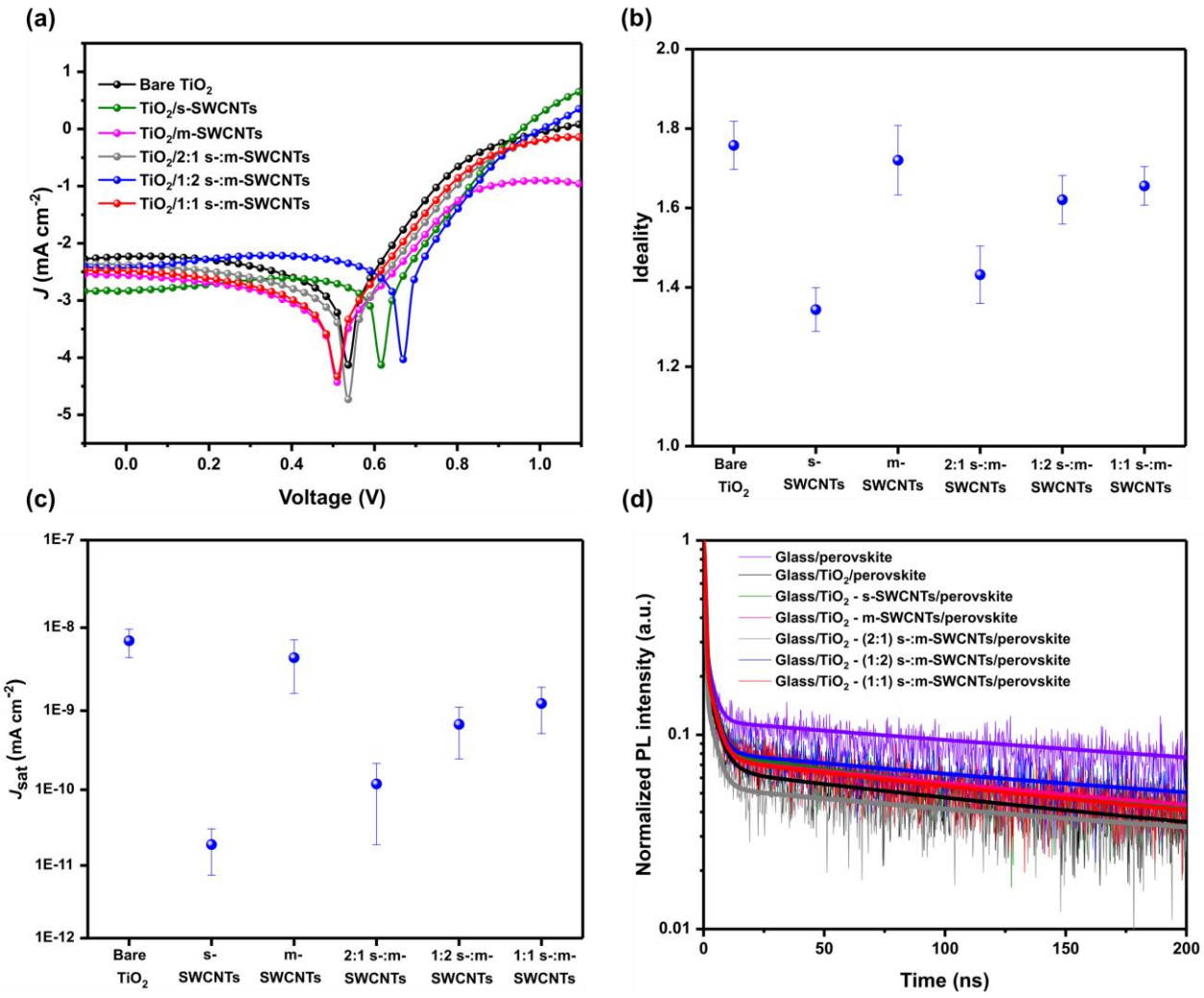

Figure S8. (a) The dark J-V characteristics, (b) the ideality factor measurements and (c) J_{sat} of the devices containing different types of SWCNTs in the TiO_2 photoelectrodes. (d) TRPL decay curves for perovskite films deposited on various substrates. Related to Figure 4

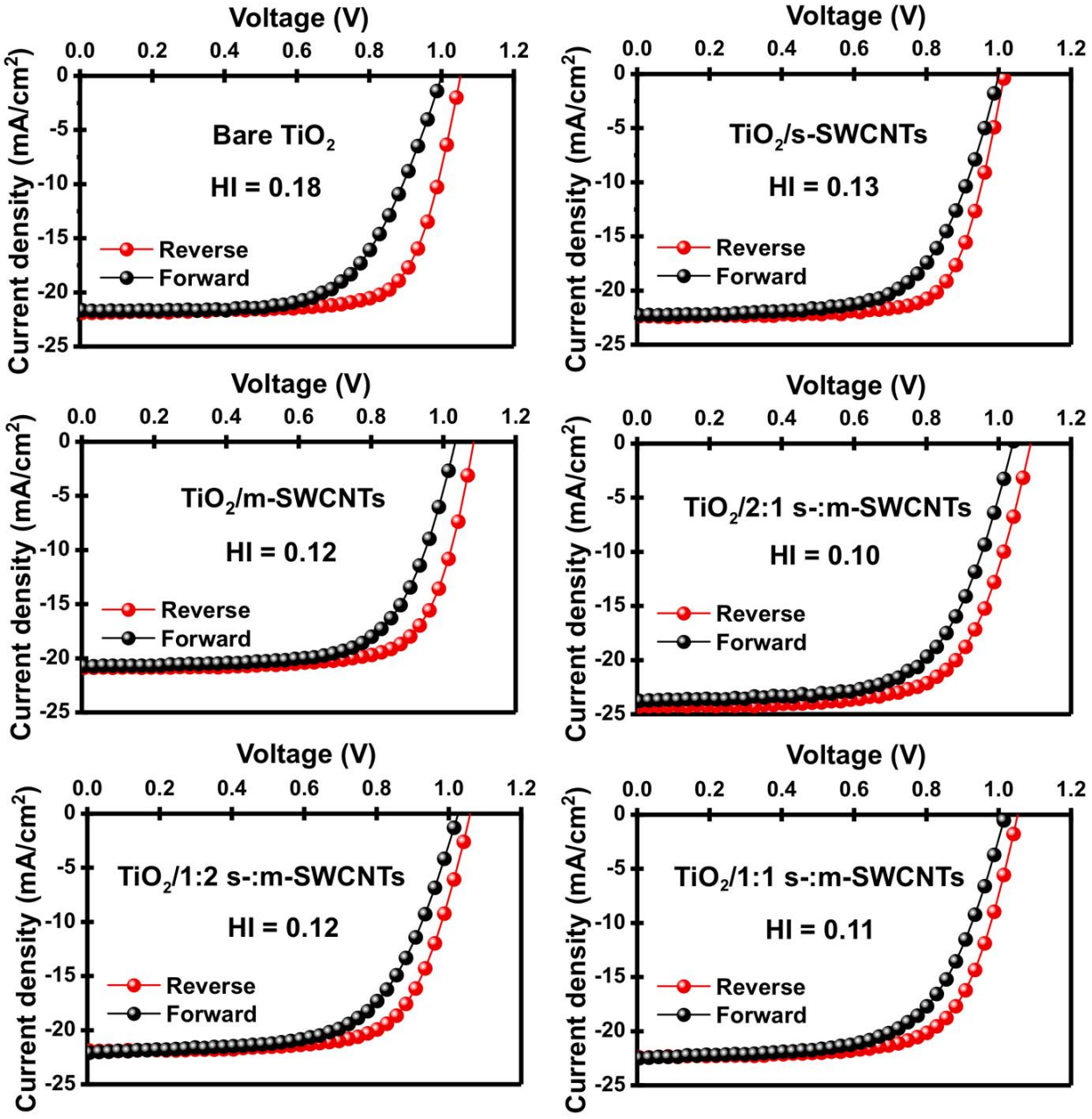

Figure S9. J-V curves measured at forward scan and reverse scan for the devices fabricated with (a) TiO_2-only, (b) TiO_2/s-SWCNTs, (c) TiO_2/m-SWCNTs, (d) TiO_2/2:1 s-:m-SWCNTs, (e) TiO_2/1:2 s-:m-SWCNTs and (f) TiO_2/1:1 s-:m-SWCNTs. Related to Figure 8.

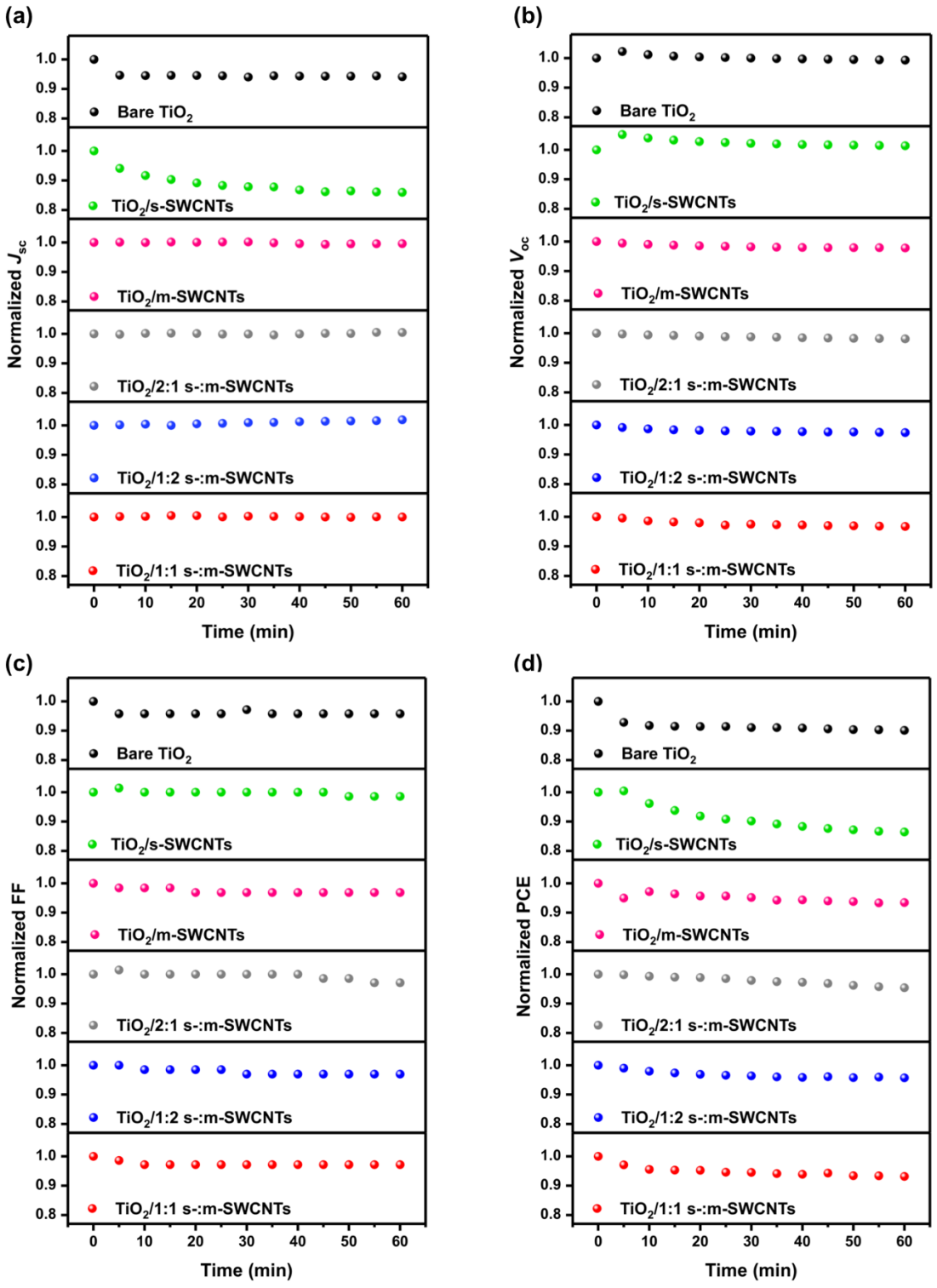

Figure S10. Light stability comparisons between the devices fabricated with and without different types of SWCNTs under 1 sun illumination condition. (a-d) Normalized J_{sc}, V_{oc}, FF,

and PCE of the PSCs showing their degradation rate during the first 60 min of age. Related to Figure 8.

DFT calculations

Theory: To obtain the atomic and electronic structure of the isolated (6, 5) CNT and the TiO_2, we perform spin-unrestricted DFT calculations with the SIESTA code (Soler et al., 2002), using the generalized gradient approximation for the exchange-correlation functional as developed by Perdew, Burke and Ernzerhof (PBE) (Perdew et al., 1996). We modelled the TiO_2 (101) surface using the slab model, which is composed of three layers of TiO_2. In the relaxation of the slab structure, we freeze the lowest layer, while the upper two layers are free to move. The SIESTA code uses basis sets comprised of numerical atomic orbitals, and approximates the atomic potential in terms of Troullier-Martins (Troullier and Martins, 1990) norm-conserving pseudopotentials. The auxiliary basis uses a real-space mesh with a kinetic energy cut-off of 500 Ry, and the basis functions are radially confined using an energy shift of 0.005 Ry (see Soler et al., 2002 for details). We allow full atomic relaxation until the forces on the atoms are less than 0.03 eV/A. All of our calculations are performed at the Γ point. The charge transfer is calculated by using the Voronoi deformation density method (Fonseca Guerra et al., 2004) as is implemented in SIESTA.

To create a supercell the combines the (6,5) CNT/(6,3) CNT and the anatase surface, we had to find a combination of the CNT and the anatase surface that would result in a supercell that is commensurate with their lattice constants. The dimensions of the TiO_2 supercell is 3.784 Å x 10.239 Å, while the lattice constant of the (6,5) CNT is 40.682 Å, and that of the (6,3) CNT is 11.289 Å. We created a supercell that combines a unit cell of (6, 5) CNT and a 3 x 4 supercell of TiO_2 (101), which yielded a lattice mismatch of 0.67% along the axis of the CNT, and a supercell

that combines a unit cell of (6,3) CNT and a 3 x 1 supercell of TiO_2 (101), which yielded a lattice mismatch of 0.57% along the axis of the CNT.

Supplemental References

Fonseca Guerra, C., Handgraaf, J. W., Baerends, E. J., and Bickelhaupt, F. M. (2004). Voronoi deformation density (VDD) charges: Assessment of the Mulliken, Bader, Hirshfeld, Weinhold, and VDD methods for charge analysis. J Comput Chem. *25*, 189-210.

Perdew, J. P., Burke, K., and Ernzerhof, M. (1996). Generalized gradient approximation made simple. Phys. Rev. Lett. *77*, 3865.

Soler, J. M., Artacho, E., Gale, J. D., García, A., Junquera, J., Ordejón, P., and Sánchez-Portal, D. (2002). The SIESTA method for ab initio order-N materials simulation. J. Phys. Condens. Matter *14*, 2745.

Troullier, N., and Martins, J. (1990). A straightforward method for generating soft transferable pseudopotentials. Solid State Commun. *74*, 613-616.